Author Manuscript

Improved Models of Ganymede's Permanent and Induced Magnetic Fields Based on Galileo and Juno Data

Xianzhe Jia[1,*], Margaret G. Kivelson[1,2], Krishan K. Khurana[2], and Raymond J. Walker[2]

1. Department of Climate and Space Sciences and Engineering, University of Michigan, Ann Arbor, MI 48109
2. Department of Earth, Planetary, and Space Sciences, UCLA, Los Angeles, CA 90095

[*] Email: xzjia@umich.edu

Key Points:

1. Obtained improved models of Ganymede's internal field by using MHD simulations to remove plasma-generated perturbations from in situ data
2. The magnitudes of the permanent dipole and quadrupole moments derived from this work do not differ significantly from previous estimates
3. Our analysis yields a reduced induction efficiency compared to prior work, placing new constraints on Ganymede's interior properties

This is the author manuscript accepted for publication and has undergone full peer review but has not been through the copyediting, typesetting, pagination and proofreading process, which may lead to differences between this version and the Version of Record. Please cite this article as doi: 10.1029/2024JE008309.

This article is protected by copyright. All rights reserved.

Author Manuscript

Abstract

Near Ganymede, the magnetic field is a superposition of Jupiter's magnetospheric magnetic field, the field arising from sources within the moon, the field generated by plasma currents driven by the interaction of flowing magnetospheric plasma with the conducting moon, and the field arising from ionospheric currents. Previous fits to Ganymede's internal field have not identified the contributions of plasma and ionospheric currents, although their contributions can obscure the signature of sources internal to the moon. Fortunately, using magnetohydrodynamic (MHD) simulations whose output agrees well with the measurements acquired on close passes by Galileo and Juno, we can estimate the moon-scale contributions of plasma sources. By subtracting the magnetic signatures of plasma and ionospheric currents from the measured field, we approximate measurements made in a current-free region. We fit the corrected data from different sets of flybys either as a sum of low order spherical harmonics or as a permanent dipole moment plus an induced dipole with approximately the same rms errors. For the induced dipole model, data from multiple flybys occurring at different phases of Jupiter's rotation are used to represent the time-variation of the external field at Ganymede. Compared with earlier estimates, the magnitude of the permanent dipole moment does not change significantly in either analysis. However, for the permanent plus induced dipole model, the induction efficiency decreases from 0.84 to ~ 0.72. The reduced efficiency places new constraints on the thickness of the ice shell above the ocean and the ocean's depth and conductivity.

Plain Language Summary

At Jupiter's moon Ganymede, several factors shape the surrounding magnetic field environment: Jupiter's own magnetic field, the moon's internal field, plasma currents arising from the moon's interaction with Jupiter's magnetospheric plasma, and currents flowing in its ionosphere. Prior models of Ganymede's internal field were based on simplified assumptions about the effects of plasma and ionospheric currents. Here we leverage computer simulations that agree well with data from close flybys made by the Galileo and Juno spacecraft to quantify the plasma-generated magnetic fields. After removing these from the measured field, we are able to improve determination of Ganymede's internal magnetic sources. We consider two types of models in fitting the observations: one model composed of a dipole and a quadrupole and the other consisting of a permanent dipole and a time-varying induced dipole. The dipole and quadrupole terms derived from our new analysis are similar to prior estimates. However, the induction efficiency for the induced dipole, which is attributed to a putative subsurface ocean, is found to be lower by ~ 10% than inferred in previous work, a result that places new constraints on key properties of Ganymede's interior, including the thickness and conductivity of the subsurface ocean.

1. Introduction

The planets and moons of the solar system are remarkably diverse in scale, composition, and appearance, so differences in their magnetic properties are to be expected. Indeed, Earth's internal field is strong enough to stand off the solar wind at 10 Earth radii and Mercury's field stands off the solar wind slightly above its surface (Korth et al., 2004), but neither Venus (Russell, 1980; Phillips and Russell, 1987) nor Mars (Acuna et al., 2001) has a global-scale magnetic field, and

This article is protected by copyright. All rights reserved.

the Moon also lacks such a field (Russell et al., 1974). It was not widely anticipated that the Galilean moons of Jupiter would be magnetized (but see Neubauer, 1978), yet measurements made by the Galileo spacecraft revealed that the largest of those moons, Ganymede, has a permanent dipole moment whose polar field is more than an order of magnitude larger than the field of Jupiter's magnetosphere (i.e., the sum of Jupiter's internally generated field and the field generated in magnetospheric plasma) in which it is embedded (Kivelson et al., 1996, 1997; Gurnett et al., 1996). None of the other moons of Jupiter and Saturn appear to generate permanent magnetic moments (Jia et al., 2010a), although inductive responses have been reported for all the Galilean moons of Jupiter (Khurana et al., 1998, 2011; Kivelson et al., 2002). Data acquired in the vicinity of Saturn's largest moon, Titan, put extremely small upper bounds (consistent with zero amplitude) on both permanent and induced fields (Wei et al., 2010).

Ganymede orbits Jupiter with a ~7.15 day period at a distance of ~15 R_J (R_J is the radius of Jupiter = 71,492 km) from Jupiter's center. At this distance, the magnitude of the field of Jupiter's magnetosphere is of order 100 nT, and its tilt differs from that imposed by the offset, tilted dipole of Jupiter as a result of currents flowing in the plasma disc external to the planet. In particular, near the centrifugal equator where plasma trapped on the field is concentrated, field lines are distended relative to dipole field lines (e.g., Connerney et al., 2020). The plasma approximately corotates with Jupiter and, because of the ~10° tilt of Jupiter's dipole field, moves up and down relative to Ganymede's nearly equatorial orbit. The ambient plasma velocity relative to Ganymede is typically ~140 km/s in the direction of Jupiter's rotation. Galileo's multiple flybys of Ganymede occurred at different phases of Jupiter's rotation (SIII phase) and hence in predictably different field and plasma environments.

Ganymede's permanent internal magnetic field, believed to be approximately stable over centuries, is generated by currents that flow in a fluid core at $r < 0.5\ R_G$ (Schubert et al., 1996; Christensen, 2015), where r is radial distance from Ganymede's center and R_G is the radius of Ganymede (R_G = 2631.2 km). The initial characterization of Ganymede's internal field relied on data from Galileo's first two passes (G1 and G2). The modeled internal dipole (Figure 1a), which reproduces the observations near Ganymede well, has an equatorial field strength of ~750 nT and a tilt angle of about 170° from the rotation axis.

Galileo's tour continued and years later Kivelson et al. (2002), hereafter referred to as MK02, added data from another pass (G28) at a SIII longitude that differed markedly from those of the first two encounters (see Table 1). The magnetospheric field at Ganymede varies with SIII longitude at the approximately 10.5 hr synodic period. The additional data made it possible either to refine the estimate of the internal moments or to identify a possible inductive contribution to the internal field. MK02 pointed out that only three (G1, G2 and G28) of the six available flybys contributed information relevant for determination of the internal field through quadrupole order. Data from three additional flybys were omitted because the measurements were obtained either too far from the surface (G7 and G29) or too close to the boundary of Ganymede's magnetosphere where strong localized currents are the dominant source of field variations (G8).

MK02 characterized the contributions to the field arising from currents flowing inside of Ganymede ($\mathbf{B_{int}}$) in two ways, either as a set of fixed internal moments through quadrupole order

This article is protected by copyright. All rights reserved.

Author Manuscript

or as a combination of a fixed dipole and an induced dipole whose orientation depends upon the direction of the instantaneous external driving field. The analysis imposed the obvious requirement that fixed internal moments be identical on all passes and that the induction efficiency (the absolute value of the ratio of the induced dipole at its pole to the driving field, taken to be in the radial direction with respect to Jupiter) be the same for all passes. Both models provided acceptable fits to the available flyby data. MK02 favored the model with magnetic induction (Figure 1b) because it provides equally satisfactory fits with fewer free parameters (five for the quadrupole model and only one for the induction model). The inferred permanent dipole has an equatorial surface strength of 719 nT, slightly smaller than the initially proposed value, and a tilt angle of $\sim 176^\circ$ with respect to the axis of rotation. The inferred induction efficiency was slightly smaller than that of a perfect conductor of the moon's size. The results were consistent with the presence of a layer of liquid water containing dissolved electrolytes buried at a depth of order 150 km beneath the surface.

With additional data from a close Juno flyby, Weber et al. (2022) fitted field measurements to both a quadrupole model and an induction model, again finding that the two models provide similarly good fits. Plattner et al. (2023) explored a range of quadrupole models, finding that they are not well constrained by available Galileo and Juno data.

Saur et al. (2015) presented complementary evidence for the existence of a subsurface ocean. They identified periodic oscillations in the orientation of Ganymede's auroral oval and argued that the amplitude of the oscillations is consistent with predictions from a model with an electrically conducting layer below the ice surface. For a subsurface ocean buried at a depth between 150-250 km, they inferred a minimum conductivity of 0.09 S/m.

Previous models of the magnetic properties of Ganymede have approximated external contributions to the measured field using the first order (n = 1) terms of a spherical harmonic expansion corresponding to a uniform external field, an approximation justified by noting that the field of Jupiter's magnetosphere does not vary significantly over spatial scales relevant to the Ganymede interaction and does not change measurably over the time of a spacecraft flyby. Previous models have used different uniform external fields to model different passes because Ganymede's magnetospheric environment changes with SIII longitude. The internal field has been modeled using low order spherical harmonics. However, plasma currents (Figure 1c) produce perturbations that modify the external field and can contribute magnetic perturbations that mimic the signature of internal fields, but previous work has neither identified nor removed such contributions.

Most spacecraft measuremenrs made in Ganymede's vicinity have been acquired well above the ionosphere. Fits to the internal field have lumped field perturbations arising from ionospheric currents together with other internal sources. It is clear that a data set from which ionospheric contributions as well as magnetospheric contributions have been removed will provide improved estimates of the internal field.

In this work, we use MHD simulations to estimate the field perturbations arising from both ionospheric currents and external plasma currents; we remove them from the data before extracting the properties of the internal magnetic field. We thereby improve on previous analyses of

This article is protected by copyright. All rights reserved.

Author Manuscript

Ganymede's internally generated spacecraft magnetic properties (MK02; Weber et al., 2022; Plattner et al., 2023) because the field that remains after removing the contribution of external current systems will be approximately curl-free. A curl-free magnetic field can be represented in terms of spherical harmonics that characterize the contributions to the field from remote external sources (Jupiter's magnetospheric field unperturbed by the presence of Ganymede) and from sources internal to the moon. The power of an expansion in spherical harmonics arises from the different symmetries and radial variations of internal and external moments. The lowest order internal spherical harmonics correspond to dipole and quadrupole moments.

Global magnetosphere simulations (e.g., Paty et al., 2006; Jia et al., 2009; Toth et al., 2016; Fatemi et al., 2016; Zhou et al., 2019; Duling et al., 2022; Romanelli et al., 2022; Stahl et al., 2023) have captured the effects of plasma currents at Ganymede with varied success (see Jia and Kivelson [2021] for a review of recent simulations of Ganymede's magnetosphere). Here we use the simulations of Jia et al. (2009), noting that the modeled field components track the measured Ganymede-scale field variations rather well.

The fitting process is iterative in the sense that it adopts previous estimates of Ganymede's internal moments and induction efficiency as input for runs of the magnetohydrodynamic (MHD) simulations. From these simulations we extract the field perturbations arising from currents flowing in the regions near the moon (Jia et al., 2009) and subtract them from the measurements. As we have noted, the remaining field is a good approximation to the field that would be measured in a current-free region near the moon (see examples shown in Olsen et al., 2010). We then fit the remaining field to low order spherical harmonics and through this iteration extract improved estimates of Ganymede's internal field, both steady and time-varying. As will be shown below, the difference between the input and output values are sufficiently small that additional iterations are not called for.

We use two different data sets to extract the properties of the internal field. Our first fits use data from the Galileo passes analyzed by MK02, an exercise that reveals how removal of the contribution of plasma currents affects the results. We repeat the procedure adding data from G8, a Galileo pass not used by MK02, and data from Juno's G34 pass. Following MK02, we model the internal field in two ways: first as a sum of internal dipole and quadrupole moments and then as the sum of an internal dipole moment plus an induced dipole moment.

2. Data Selection

During its eight years in orbit around Jupiter, Galileo acquired magnetometer data (Kivelson et al., 1992, 2022) on six close passes by Ganymede. On June 7, 2021, the Juno spacecraft provided additional magnetic field measurements (Connerney et al., 2017; Connerney, 2017) from a pass with closest approach < 0.4 R_G from the moon's surface (Hansen et al., 2022). No further passes are anticipated until the next decade when both the Europa Clipper and the Juice missions plan flybys followed by insertion of Juice into orbit around Ganymede.

In Figure 2a we illustrate the range of Ganymede longitude/latitude over which the Galileo and Juno passes occurred, highlighting the portions of those passes that were within 2 R_G of the the moon's center. In Figure 2b we illustrate the location of the different passes relative to Jupiter's

This article is protected by copyright. All rights reserved.

Author Manuscript

magnetic equator. It is critical for the assessment of an inductive response to include data from passes acquired both above (radial component of the field positive) and below (radial component of the field negative) the magnetic equator.

For analysis of the internal field, it is desirable to focus on passes that acquired data at low altitudes with significant field magnitude variation. Table 1 shows the time spent within 2 R_G of Ganymede's center of mass and the range of field magnitudes (maximum minus minimum) recorded during that time. Aditional entries note the closest approach altitude and the System III (SIII) west longitude of the encounters. Passes G1, G2, and G28 and Juno G34 acquired data close to Ganymede for 7 or more minutes and recorded field magnitude changes of hundreds of nT. Pass G7 never came within 2 R_G of Ganymede's center. Pass G29 acquired data within 2 R_G for about 6 minutes but it recorded only 55 nT variation of field magnitude. Passes G1, G2, and G28, previously analyzed by MK02, span the magnetospheric equator and provide information that is useful for establishing parameters of the internal field, although they give limited coverage in two quadrants of Ganymede (see Figure 2a). Pass G8 provided measurements in one of the missing quadrants and filled in a gap in synodic phase but recorded little change in field magnitude. It encountered Ganymede in the center of the plasma sheet where external conditions are disturbed and remained close to Ganymede's magnetopause where effects of plasma currents are strong. The G8 data can be useful in establishing the internal field only after removing the contributions of plasma currents to the measured field. The Juno G34 pass recorded significant changes in field magnitude during its 7 minutes within 2 R_G of Ganymede and its closest approach on the Jupiter-facing side of the moon improved spatial coverage.

3. MHD Simulations of Close Passes by Ganymede

In a series of papers, Jia and colleagues describe the details of their three-dimensional resistive MHD simulations used to model the plasma and field environment of Ganymede (Jia et al, 2008, 2009, 2010b). The code is run using a non-uniform spherical mesh that provides high spatial resolution in regions of rapid spatial variations of plasma and field properties. The semi-implicit scheme adopted for time-stepping removes short-wavelength, high-frequency variations. At Ganymede, the upstream field and plasma conditions are relatively steady and predictable (see Figure 2 in Kivelson et al., 1996). Spacecraft measurements prior to and following each individual encounter with the magnetosphere provide realistic input values of the density, velocity, and field values (Kivelson et al., 2004; Allegrini et al., 2022; Weber et al., 2022) for the upstream outer-boundary conditions in the corresponding run of the MHD model. The downstream outer boundary at 40 R_G is remote from Ganymede and is set to be non-reflecting. Properties of Ganymede's ionosphere such as its conductivity are poorly constrained observationally. In developing the MHD models used in this analysis, Jia et al. (2009) selected a model representing an ionosphere with finite Pedersen conductance of a few Siemens, whose results quite closely track the measured global scale variations relevant to low order estimates of the internal field (Jia et al., 2009). The simulations were run in GphiO coordinates in which the *X*-axis is along the direction of corotation at the time of Galileo's closest approach to the satellite, the *Z*-axis is parallel to the Jovian spin axis and *Y* completes the right-handed set (positive towards Jupiter).

This article is protected by copyright. All rights reserved.

Author Manuscript

As pointed out in Jia et al. (2010b), both data and models may exhibit temporal variations on time scales shorter than the time interval required for a spacecraft to cross the magnetosphere and its disturbed surroundings or for the ambient flow to pass by the interaction region, even though upstream conditions are nearly steady over the duration of a flyby. The situation differs considerably from that for planetary magnetospheres for which upstream conditions are rarely steady over times relevant to the interaction, such as the time for the solar wind to flow by. It seems that for the sub-Alfvénic flow incident on Ganymede, dynamical processes such as reconnection are unsteady even under stable external conditions and the system does not reach a fully time-stationary state. Correspondingly, the simulation results do not reach a fully time-independent state because rapid temporal variations arising from reconnection on the upstream magnetopause (typically on a scale too small to affect estimates of the structure of low order internal moments) persist after the large-scale results become steady (Jia et al., 2010b; Zhou et al., 2020).

Figures 3 and 4 show magnetic field components measured along the trajectories of Galileo flybys G2 and G28 and the values extracted from the MHD simulations for the same two flybys (Jia et al., 2009, 2010a). Both figures show time-averaged simulation results obtained by first extracting the simulated magnetic field along a fixed spacecraft trajectory from the model at multiple time steps and then averaging the outputs over time steps that span a time interval of ~ 2 minutes after the system stabilizes. The 2-minute time window chosen for time-averaging corresponds roughly to the typical flow convection time across the magnetospheric region at Ganymede. As shown in Figures 3(a) and 4(a), the simulations successfully reproduce the low order features of the measurements including the location of the magnetopause and the dominant jumps at boundary encounters and thus appear to provide useful approximations to the effects of global scale plasma currents.

The input ($\mathbf{B_{sim}^{t=0}}$) field in the MHD model consists of the background field $\mathbf{B_J}$ (Jupiter's magnetospheric field) and Ganymede's internal field $\mathbf{B_{int}}$, including both the permanent and the induced dipole moments given by MK02. The difference between the simulated fields ($\mathbf{B_{sim}^{t}}$) and the input field ($\mathbf{B_{sim}^{t=0}}$) observed along the spacecraft trajectory provides a good approximation to the perturbation field arising from plasma currents ($\mathbf{B_{plasma} = B_{sim}^{t} - B_{sim}^{t=0}}$), which includes contributions from both magnetospheric ($\mathbf{B_{above}}$)and ionospheric ($\mathbf{B_{below}}$) currents. Figures 3(b) (for G2) and 4(b) (for G28) show the simulated perturbation field associated with plasma currents around closest approach. All three components of the field during the interval around C/A exhibit variations, which arise because the contributions from magnetopause and ionospheric currents change significantly over relatively small spatial scales. As a result, for both flybys, the perturbation fields extracted from the MHD model deviate markedly from the uniform field previously used to represent the external field in fits to the data.

We have run the MHD model for each of the Galileo passes and the Juno G34 pass near Ganymede. The simulations for the additional passes also accord closely with the observations on spatial scales of order 0.2 R_G or longer and time scales of minutes (Jia et al., 2008, 2009, 2010b; Jia and Kivelson, 2021), thus providing good approximations to the features of the magnetic environment pertinent to fitting the internal field. In particular, the magnetopause currents,

This article is protected by copyright. All rights reserved.

Author Manuscript

responsible for the abrupt variations of field components inbound and outbound from closest approach, are captured for all passes.

In the following, we describe how we use our MHD simulations to improve estimates of the properties of the internal field. For the Galileo passes analyzed by MK02, we use the same time intervals that they used for fitting the internal field (see Table II in MK02), allowing us to establish how the removal of plasma-generated fields modifies the estimates. To better constrain the properties of the internal field, we repeat our analysis adding analogous data segments from an additional Galileo pass (G8) and from the Juno flyby. From the measurements $(\mathbf{B_{obs}})$, we subtract the background field of Jupiter's magnetosphere $(\mathbf{B_J})$ obtained from a polynomial fit to the field components measured before and after the encounter and the external perturbation fields arising from plasma currents ($\mathbf{B_{plasma}}$) modeled by sampling our simulations along the flyby trajectory. We assume that the residuals arise completely from current sources $(\mathbf{j_{int\ to\ G}})$ internal to the moon. Then, following MK02, we fit the residuals to combinations of a permanent dipole and either permanent quadrupole moments or an induced dipole. The fitting procedure follows that described in MK02 except that in our analysis, we have used estimates from our MHD simulations to remove magnetic perturbations arising from plasma sources from the measured field.

We use pass-specific approaches in dealing with space-time aliasing of the model and of observations. For the G1, G2, G8 and Juno G34 flybys, following the same time-averaging approach as described above we average simulation output over multiple time steps (spanning a time interval of ~ 2 minutes after the system stabilizes) to obtain a reasonably good representation of the large-scale magnetic field seen along the spacecraft trajectory. The field measured on the G1 and G2 flybys varied smoothly throughout the close encounter. However, the field measured on the G28 flyby, which remained close to the upstream magnetopause, fluctuated in response to the dynamics of the magnetopause (Jia et al., 2010b). In order to take the associated temporal variability into account, we first fit model data extracted along the flyby trajectory from each time step (130 time steps in total) of the G28 simulation together with data from other flybys (e.g., G1, G2, G8 and Juno G34), and then extract the best fit from the distribution of model parameters by averaging the fitted parameters over the simulation time steps that follow the establishment of a quasi-steady state, which, as will be shown below, typically occurs after ~ 70 simulation time steps that correspond roughly to the flow convection time across the magnetosphere.

4. Solving for External and Internal Fields as Spherical Harmonics

For slowly varying fields, Ampere's law (in SI units) reduces to

$$\nabla \times \vec{\mathbf{B}} = \mu_0 \vec{\mathbf{j}} \tag{1}$$

where $\vec{\mathbf{B}}$ and $\vec{\mathbf{j}}$ are the magnetic field and the current density, respectively, and μ_0 is the permeability of free space. In current-free regions, Ampere's law becomes $\boldsymbol{\nabla} \times \vec{\mathbf{B}} = 0$ and the magnetic field $\vec{\mathbf{B}}$ becomes the negative gradient of a scalar potential, V. Gauss's law requires $\boldsymbol{\nabla} \cdot \vec{\mathbf{B}} = 0$ and, consequently, V is a solution of Laplace's equation, $\nabla^2 V = 0$.

This article is protected by copyright. All rights reserved.

Author Manuscript

The magnetic field of a spherical body can be described in spherical coordinates $[r, \theta, \varphi]$. We use *Gsph*, a Ganymede-centered coordinate system in which θ is an angle relative to the rotation axis of Ganymede and φ is the azimuthal angle about that axis measured from the direction between Ganymede's center of mass and Jupiter's center of mass following right-handed convention. If no currents are present in a region of radius $a < r < c$, it is appropriate to expand the potential V and the magnetic field $\vec{\mathbf{B}} = -\boldsymbol{\nabla} V$ in a series of spherical harmonics. Solutions of Laplace's equation in spherical harmonics include terms with radial dependences of $1/r^{n+1}$ (arising from internal sources) and r^n (arising from external sources).

$$V = V^{\text{int}} + V^{\text{ext}}$$

$$= R \sum_{n=1}^{N_{int}} \sum_{m=0}^{n} \left(g_n^m \cos m\varphi + h_n^m \sin m\varphi\right) \left(\frac{R}{r}\right)^{n+1} P_n^m(\cos\theta) \tag{2a}$$

$$+ R \sum_{n=1}^{N_{ext}} \sum_{m=0}^{n} \left(G_n^m \cos m\varphi + H_n^m \sin m\varphi\right) \left(\frac{r}{R}\right)^{n} P_n^m(\cos\theta) \tag{2b}$$

(Chapman and Bartels, 1940; Langel, 1987), where R is a reference radius (typically chosen to be the radius of the obstacle of interest), P_n^m are the associated Schmidt semi-normalized Legendre functions, N_{int} is the maximum degree and order of the internal potential coefficients g_n^m, h_n^m, and N_{ext} is that of the external potential coefficients G_n^m, H_n^m.

Correspondingly, the magnetic field $\vec{\mathbf{B}} = \left(B_r, B_\theta, B_\varphi\right)$ becomes:

$$B_r = -\frac{\partial V}{\partial r} = \sum_{n,m} \left[(n+1)\left(g_n^m \cos m\varphi + h_n^m \sin m\varphi\right) \left(\frac{R}{r}\right)^{n+2} \right.$$

$$\left. - n\left(G_n^m \cos m\varphi + H_n^m \sin m\varphi\right) \left(\frac{r}{R}\right)^{n-1} \right] P_n^m(\cos\theta) \tag{3}$$

$$B_\theta = -\frac{1}{r}\frac{\partial V}{\partial \theta} = -\sum_{n,m} \left[\left(g_n^m \cos m\varphi + h_n^m \sin m\varphi\right) \left(\frac{R}{r}\right)^{n+2} \right.$$

$$\left. + \left(G_n^m \cos m\varphi + H_n^m \sin m\varphi\right) \left(\frac{r}{R}\right)^{n-1} \right] \frac{dP_n^m(\cos\theta)}{d\theta} \tag{4}$$

$$B_\varphi = -\frac{1}{\text{r}\sin\theta}\frac{\partial V}{\partial \varphi} = \sum_{n,m} m \left[\left(g_n^m \sin m\varphi - h_n^m \cos m\varphi\right) \left(\frac{R}{r}\right)^{n+2} \right.$$

$$\left. + \left(G_n^m \sin m\varphi - H_n^m \cos m\varphi\right) \left(\frac{r}{R}\right)^{n-1} \right] \frac{P_n^m(\cos\theta)}{\sin\theta} \tag{5}$$

The first order (n = 1) terms in the spherical harmonic expansion have a simple geometric meaning. For n = 1 , the magnetic field of external origin is independent of radius, i.e., it is uniform. It is convenient to describe such a uniform field in a Cartesian coordinate system, for example, the GphiO coordinate system described above. The first-order coefficients of the external field are

This article is protected by copyright. All rights reserved.

Author Manuscript

then related to the vector components as follows: $G_1^0 = -B_z, H_1^1 = B_x$ and $G_1^1 = -B_y$. The first order (n = 1) terms arising from internal sources (dipole moments) are related to the vector components in GphiO coordinates by $g_1^0 = M_z$ (represents a centered dipole aligned with the spin or $\hat{z}$-axis) $h_1^1 = -M_x$ (represents a centered dipole in the equatorial plane aligned with the $-\hat{x}$-axis) and $g_1^1 = M_y$ (represents a centered dipole in the equatorial plane aligned with the $\hat{y}$-axis).

A surface that separates external and internal field sources is defined by the altitude at which the spacecraft acquired measurements rather than the surface of the obstacle. Consequently, as we have noted, the field perturbations arising from currents between the spacecraft and the surface, such as the currents flowing in the ionosphere, appear as internal sources even though they result from currents flowing external to the moon.

In order to use spacecraft measurements to determine the internal field, one can express the magnetic field given in equations (3) to (5) as $\mathbf{Ax} = \mathbf{b}$, where $\mathbf{b}$ are the magnetic field measurements (in region $a < r < c$), $\mathbf{x}$ contains the coefficients of the spherical harmonic expansion and $\mathbf{A}$ is a matrix composed of geometric factors that characterize the spatial locations of the observations. If there are n magnetic field measurements and each measurement consists of three vector components in spherical coordinates, then $\mathbf{b}$ is a $3n \times 1$ matrix. If the fit to the internal field is carried out through terms of order m, then the number of spherical coefficients is $M = \sum_{l=1}^{m}(2l+1)$ and $\mathbf{x}$ is an $M \times 1$ column matrix while $\mathbf{A}$ is a $3n \times M$ matrix.

Our interest is to find $\mathbf{x}$, which contains information about the internal field, by solving an inverse problem for a given $\mathbf{b}$. We can use several inversion approaches to invert $\mathbf{x}$. We adopt a version of a widely used approach, a least squares fitting in which the optimal model parameter $\mathbf{x}$ is obtained by minimizing the square sum of the residuals, $\mathbf{E} = \mathbf{e^T e}/2$, where $\mathbf{e} = (\mathbf{b} - \mathbf{Ax})$ represents the residuals between the observations and the model predictions and $\mathbf{e^T}$ is the transpose of $\mathbf{e}$. By setting $\mathrm{d}\mathbf{E}/\mathrm{d}\mathbf{x} = 0$, one obtains

$$\mathbf{x} = (\mathbf{A^T A})^{-1}\mathbf{A^T b} \tag{6}$$

Because the close flybys used in the inversion differ in altitude and maximum field strength, a least-square fit to the full data set using equation (6) would be biased towards fitting the lowest altitude passes. In order to optimize the fit, we follow the approach of weighted least squares fit presented in MK02 by weighting the contributions of the i-th flyby inversely by $B_{max}^i / \sqrt{(\sum_i B_{max}^i)^2}$, where B_{max}^i is the maximum field strength used in the fitting for that flyby. Correspondingly, the square sum of the weighted residuals becomes $\mathbf{E} = \mathbf{e^T W^2 e}/2$, where $\mathbf{W}$ is a diagonal weighting matrix with elements $w_i = 1/B_{max}^i$. The solutions to the weighted least squares fit are then given by

$$\mathbf{x} = (\mathbf{WA^T WA})^{-1}\mathbf{WA^T Wb} \tag{7}$$

A useful metric for assessing the goodness of a model fit is the root-mean-square (***rms***) error between the model fit ($\mathbf{B_{fit}}$) and the data, which, in this case, is the measured field with the background and plasma-perturbation fields subtracted. The rms is defined as

This article is protected by copyright. All rights reserved.

$$\boldsymbol{rms} = \sqrt{\frac{1}{3N}\sum_{j=1}^{N}\left\|\left[\mathbf{B_{obs}} - \mathbf{B_J} - \mathbf{B_{plasma}}\right] - \mathbf{B_{fit}}\right\|^2} \tag{8}$$

where N is the number of magnetic field vectors used in fitting the model.

As shown in later sections, for each internal field model examined in this study we have calculated the *rms* errors for individual passes as well as total *rms* errors summed over all passes used in the model fit. The total *rms* error without weighting is defined as

$$\boldsymbol{Total\ rms} = \sqrt{\frac{1}{3\sum_i N_i}\sum_i\left(\sum_{j=1}^{N_i}\left\|\left[\mathbf{B_{obs}} - \mathbf{B_J} - \mathbf{B_{plasma}}\right] - \mathbf{B_{fit}}\right\|^2\right)} \tag{9}$$

The total weighted *rms* error is given by

$$\boldsymbol{Total\ weighted\ rms} = \frac{\sqrt{\frac{1}{3\sum_i N_i}\sum_i w_i^2\left(\sum_{j=1}^{N_i}\left\|\left[\mathbf{B_{obs}} - \mathbf{B_J} - \mathbf{B_{plasma}}\right] - \mathbf{B_{fit}}\right\|^2\right)}}{\left(\sum_i w_i\right)/N_{pass}} \tag{10}$$

where $w_i = 1/B_{max}^i$ is the weighting function dependent on the maximum field strength of the i-th pass and N_{pass} is the total number of passes used in the fitting.

5. Perturbations Arising from Plasma Currents

As noted above, we can estimate the low order field perturbations arising from plasma currents that obscure the signatures of internal fields by using MHD simulations run for conditions of different spacecraft flybys.

The total field ($\mathbf{B_{obs}}$) with the background Jovian magnetospheric field ($\mathbf{B_J}$) subtracted relates to the fields arising from distinct current sources, which we write as

$$\begin{aligned}\nabla \times (\mathbf{B_{obs}} - \mathbf{B_J}) &= \nabla \times \left(\mathbf{B_{int}} + \mathbf{B_{plasma}}\right) \\ &= \nabla \times (\mathbf{B_{int\ to\ G}} + \mathbf{B_{below}} + \mathbf{B_{above}})\end{aligned} \tag{11}$$

where $\mathbf{B_{int\ to\ G}}$, $\mathbf{B_{below}}$, and $\mathbf{B_{above}}$ are the field perturbations arising from currents flowing inside of the moon, currents flowing outside the moon but below the altitude of the spacecraft trajectory, and currents flowing at and above the altitude of spacecraft trajectory, respectively. Estimates of $\mathbf{B_{below}}$ and $\mathbf{B_{above}}$ extracted from the MHD model along the trajectory of the spacecraft provide the desired approximation to the field that would have been present in the absence of local plasma currents and ionospheric currents.

5.1 Field Models Based on the G1, G2, and G28 Passes

The MK02 estimates of the internal field used data from flybys G1, G2 and G28 without correcting for plasma effects. In order to establish how the estimates of internal sources change after correcting for plasma contributions, we first use data from the same three flybys to obtain fits to the internal field. As in the earlier work, we fit the internal field both to a permanent dipole plus an induced dipole whose orientation and magnitude changes are proportional to the external field of the Jovian magnetosphere at the time of the close pass and to a dipole plus quadrupole terms. Specifically, in fitting the induced dipole, we follow the approach used in MK02 by representing

This article is protected by copyright. All rights reserved.

Author Manuscript

the external driving field as the *y*-component at closest approach of a third-order polynomial fit to the background field measured outside of about 5 R_G. It is interesting to note that the background field obtained through our polynomial fit is within ~ 2 nT of the value predicted by the JRM33 internal field model (Connerney et al., 2022) plus the CON2020 current disc model (Connerney et al., 2020) for all close flybys except G28. For G28, the JRM33+CON2020 model predicts a noticeably weaker B_r (by about 15 nT) than the polynomial fit. The reason for this discrepancy remains unknown, although it is possible that changes in the external solar wind conditions may have influenced the configuration of Jupiter's magnetosphere during the G28 flyby.

We assume that the time-varying component of the external field is dominated by the synodic-period variation, ignoring small-amplitude contributions from such periodicities as Ganymede's orbital period and harmonics of the synodic period (e.g., Seufert et al., 2011). The locations of Ganymede in SIII (west) longitudes for the different flybys are provided in Table I. The radial field of Jupiter's magnetosphere was close to its maximum positive value during passes G1 and G2 and close to its maximum negative values during pass G28. Thus the three passes provide samples of the variations imposed on Ganymede at its synodic period. We run the simulation for conditions appropriate to each of the intervals sampled and use the outputs (linked to their synodic phases) to represent the changes of the field near Ganymede at the synodic period. In fitting the limited data available, we make different assumptions about the nature of the internally generated field, referring to dipole plus quadrupole (permanent fields) as MagModel1 and to dipole plus induced response as MagModel2. We further assume that there is no phase lag between the inducing field and the induced field. As will be shown later, this assumption is justified for the parameter regime of interest.

5.1.1 MagModel1: Permanent Dipole Plus Induced Dipole

Our fits to an internal field model ($\mathbf{B_{fit}}$) consisting of a permanent dipole and an induced dipole are illustrated in Figure 5, which shows the fitted dipole coefficients and the induction efficiency [panels (a) – (d)] vs. timestep of the G28 simulation. Panel (e) shows the *rms* error of the model fit as a function of simulation time step for data acquired on individual passes and for the full data set. The *rms* errors of MK02 are blue dashed lines. As noted earlier, following time step 70 (the interval shaded in the plot), models of the G1 and G2 passes are quite stable in time and well represented by their values at any fixed time step, but the model for G28 varies in time even after its average value has stabilized. As we have remarked, G28 was an upstream pass that came relatively close to the magnetopause and the continued small amplitude variations arise from dynamics on the magnetopause (Jia et al., 2010b). For that reason, Figure 5 represents the parameters obtained from a fit to data output from a nominal time step in the G1 and G2 simulations (after the system stabilizes) but shows fits from different time steps in the G28 simulation.

The time profiles shown in Figure 5 clearly indicate two stages of the G28 simulation. Prior to ~ 70 time steps (the initialization stage in the unshaded region), the results evolve gradually and smoothly with time. After ~ 70 time steps (shaded region), the system has settled into a quasi-steady state where the large-scale structure of the magnetosphere has formed in the simulation but

This article is protected by copyright. All rights reserved.

Author Manuscript

small fluctuations around a relatively steady mean are present due to magnetospheric dynamics associated with unsteady reconnection. For example, the fitted induction efficiency during the interval after the system stabilizes (shaded region) varies between 0.66 and 0.77, with a mean value of 0.72. We can examine its variations by comparing the mean value averaged over the first half of the shaded region, which amounts to 0.706, to that for the second half of the interval, which is 0.723. The change between the first and second halves of the shaded region is only about 2% and both of these mean values fluctuate around the total mean (0.715) at 1% level, which we deem insignificant. Recognizing that the time duration in the shaded region corresponds roughly to the flow convection time across the magnetosphere, we think it unlikely that further temporal variations would signifincantly change the inferred induction efficiency.

Table 2 lists averages of the fitted parameters from MagModel1 over timesteps in the gray-shaded interval of Figure 5 and compares the fitted parameters with those obtained by MK02. The dominant component of the dipole, g_1^0 (or M_z), is slightly larger in MagModel1 than in MK02 and the two minor dipole components, g_1^1 and h_1^1, are smaller. Correspondingly, the induction efficiency [panel (d)] decreases from 84% in MK02 to about 72%, which corresponds to the mean value averaged over multiple time steps of the G28 simulation. Because induction efficiency bears on the properties of an ocean buried beneath an icy crust, this reduction is significant. Compared with results of MK02, the *rms* errors of the fits to data from the G1 and G2 passes increase, whereas the *rms* error of the fit to data from the G28 pass decreases. The total *rms* error calculated for all three passes is nearly the same as that reported by MK02, whereas the total weighted *rms* error is considerably smaller than the MK02 model. We discuss these results more fully in Section 7 where we compare multiple models.

5.1.2. MagModel2: Dipole Plus Quadrupole

Using data from passes G1, G2, and G28, we fit the internal field to dipole and quadrupole moments, assuming no inductive response. We have plotted the model results, including three dipole coefficients and five quadrupole coefficients along with the *rms* errors in Figure 6. Table 2 summarizes the results and compares them with those of MK02. The magnitude of the dominant dipole component, g_1^0, is larger than those obtained in MagModel1 and MK02. The magnitudes of the two minor dipole components, g_1^1 and h_1^1, are smaller in MagModel2 than in MK02. The quadrupole coefficients also differ in the two models. The dominant quadrupole component in MagModel2 is h_2^1, whereas the largest quadrupole component in MK02 is g_2^1. However, the quadrupole terms are all quite small in both models. Both the total *rms* error and the *rms* errors for individual passes, especially for the G1 and G28 passes, are smaller in MagModel2 than in MK02.

Our fits to the passes used by MK02 show that correction for plasma effects changes the estimates of the internal dipole moment a little by modifying its tilt slightly. However, the estimates of induction efficiency and of quadrupole moments change significantly.

5.2 Models Based on the G1, G2, G8, G28 and Juno Passes

Previous analyses, including those of Section 6.1, did not use data from Galileo's G7, G8, and G29 passes. Table 1 shows that G7 did not come close enough to Ganymede to provide data useful

This article is protected by copyright. All rights reserved.

Author Manuscript

for assessing the internal field and that G29 recorded a range of field values too small to be useful in establishing properties of the internal field. G8 measurements, despite their relatively small range of variation, are especially significant in establishing properties of the internal field because closest approach occurred in a quadrant not covered by any other flyby (see Figure 2a). However, this pass was close to the magnetopause where plasma effects are significant. Unless corrected for plasma effects, data from this pass would not improve our estimates of the internally generated fields. Fortunately, our MHD simulations, which represent the measurements quite closely, can provide a good estimate of the dominant plasma effects (e.g., Jia et al., 2009), allowing us to remove a good approximation to the field perturbations arising from plasma currents. The Juno flyby of Ganymede in June of 2021 also provided useful data. In the next sections we describe fits to both dipole plus quadrupole sources and to dipole plus induction sources using data from the Galileo G1, G2, G8, G28 and the Juno G34 passes from which we have removed the contributions from plasma sources.

5.2.1 MagModel3: Permanent Dipole Plus Induced Dipole

MagModel3 uses data from passes G1, G2, G8, G28, and Juno-G34 to fit internal sources as a permanent dipole and an induced dipole. For the G8 and Juno-G34 flybys, we modeled the external driving field using the approach described in Section 6.1. Figure 7 shows the fitted parameters, again using data from multiple time steps of the G28 simulation. The fitted induction efficiency in this model varies between 0.65 and 0.76, with a mean of 0.71, during the interval after the system stabilizes (shaded region in Figure 7). Table 2 shows the averaged model parameters over the time steps shaded with grey in Figure 7. Figure 7 and Table 2 also display the internal field parameters of MagModel1, revealing that the parameters of the internal field changed little from adding measurements from more passes, although the tilt implied by the value of h_1^1 is closer to the MK02 result than to MagModel1. The *rms* errors for individual passes and for the summed total (both weighted and unweighted) are very close to the results of MagModel1, and both models have smaller total weighted *rms* errors than MK02, although the difference is probably not significant.

5.2.2 MagModel4: Dipole Plus Quadrupole

With data from five passes, we also fit an internal field model of a dipole plus a quadrupole. Figure 8 and Table 2 show the model results and compare them with MagModel2 and MK02. The dipole coefficents in MagModel4 are similar to MagModel2, both having larger g_1^0 and smaller g_1^1 *and* h_1^1 than MK02. The quadrupole terms in MagModel 4 remain small compared to the dipole, although their values differ slightly from the other two models.

6. Discussion

We have used the outputs from global MHD simulations, which were run with an assumed internal field model from MK02, to determine the magnetic field perturbations arising from plasma currents. We then removed the field perturbations from the measured field and fit the remaining field to obtain improved internal field models. In principle, an iterative approach would be desirable to address such an inversion problem. However, as shown in our Table 2, the differences in the fitted internal moments between the previous models (MK02) and our new models are small

This article is protected by copyright. All rights reserved.

Author Manuscript

and would result in minimal changes to the magnetic perturbations arising from external currents. For example, MagModel1 gives an induction efficiency of 0.72 and a permanent dipole moment of 724 nT·R_G^3. Assuming the maximum strength of ~ 100 nT for the driving field at the synodic period predicted at Ganymede's orbit (e.g., Fig. 6 in Kivelson et al. [2002]), the induced dipole moment is 36 nT·R_G^3, oriented in the direction radial to Jupiter, which when superimposed onto the permanent dipole that lies largely along the Z-axis, would lead to an effective total internal dipole moment of 725 nT·R_G^3. In comparison, the same permanent plus induced dipole model in MK02 gives a total dipole moment of 720 nT·R_G^3. The difference in dipole field strength between the two models is only 0.7%. To assess the significance of changes in the internal field in affecting the external currents, a useful metric is the location of the upstream magnetopause. For fixed upstream pressure, a 0.7% change in Ganymede's internal dipole strength would result in $(0.7\%)^{\frac{1}{3}} \approx 0.2\%$ change in the standoff distance of the upstream magnetopause. Therefore, we believe that the new internal field values would produce insignificant changes to the modeled global configuration and current systems of Ganymede's magnetosphere. For this reason, we think it unnecessary to iterate the MHD simulations with the updated internal field models.

Table 2 reveals that models using MHD simulations to represent and remove external field perturbations yield a larger g_1^0, a slightly smaller g_1^1 and a smaller h_1^1 than models that approximate the perturbation fields arising from external sources as uniform fields (MK02). On the other hand, the dipole moments in the four models are quite consistent with each other, suggesting that these estimates are robust. For the two models using data with the most complete coverage (MagModel3 and MagModel4), the fitted permanent dipole has equatorial surface strengths of 720 nT and 727 nT, respectively, with very similar tilts from the spin axis (176° and 177°, with the pole in the southern hemisphere) and rotation from the Jupiter-facing meridian towards the trailing hemisphere (14.8° and 10.9°). For comparison, the MK02 dipole has an equatorial surface strength of 719 nT with a tilt of 176° rotated ~24° from the Jupiter-facing meridian towards the trailing hemisphere.

The *rms* errors differ little between the model of a permanent dipole plus an induced dipole and the model of a dipole plus a quadrupole. In the Appendix, we present the correlation coefficients for various model parameters and point out that the multipole fit is not well constrained by the available data, as noted by Plattner et al. (2023). The Galileo magnetometer was operated in the high range mode (±16000 nT) during Ganymede flybys. The sensor resolution in this mode is 0.5 nT (Kivelson et al., 1992). The data, therefore, cannot distinguish between models that have *rms* error differences less than 1 nT (e.g., between MagModel3 and MagModel4 in Table 2). However, echoing MK02, we propose the success of the one-parameter induction model in fitting the data almost as well as the quadrupole model makes it probable that the internal field of Ganymede is the sum of a permanent dipole field (generated in the deep core) and an induced field (generated in a layer of melt within the icy crust).

The induction efficiency is effectively the same in models MagModel1 and MagModel3, and is less than that of MK02, implying that there is a weak contribution of dipole symmetry arising from plasma currents. Let us consider the implication of a 72% induction efficiency for the properties of the conducting region. MK02 noted that an induction response efficiency less than

This article is protected by copyright. All rights reserved.

Author Manuscript

unity can be understood if the region of high conductivity is buried beneath the surface. The magnitude of an induced field falls with the cube of the radial distance from the surface of the conducting shell. By assuming extremely high conductivity (essentially a perfect conductor), one can calculate the maximum depth of a buried conductor consistent with the proposed induction efficiency. A highly conducting layer buried at depth $\left(1-(0.72)^{1/3}\right)R_{\mathrm{G}} \approx 273$ km could account for the reduction of the induced field signal to 72% of its maximum value. Noting that temperature increases with depth in Ganymede's interior, it is reasonable to identify the buried conducting region as a layer of melted ice, i.e., an ocean beneath an ice crust. However, this large a depth of burial is improbable. Both temperature and pressure increase with depth in Ganymede's interior, and pure water ice would melt at a depth of ~ 150 – 170 km (Schubert et al., 1986; Kivelson et al., 2002). Recent microwave radiometer measurements from the Juno spacecraft yielded an independent constraint on Ganymede's ice shell thickness with an upper limit of 150 km (Brown et al., 2023). Thus, it seems probable that the ocean surface lies less than 150 km beneath the surface and that the ocean conductivity is less than 1 S/m.

In Figure 9, we use the approach of Zimmer et al. (2000) to evaluate the dependence of the ocean thickness on the ocean conductivity for a range of plausible ice shell thicknesses (25 km to 250 km), assuming that the normalized amplitude of the response to a 10.5 hr period driving signal is 0.72. If the surface of the melt is located at a depth of ~ 150 km, the 72% induction efficiency places a constraint on the conductivity and thickness of the melted layer. The minimum conductivity required to account for a 72% induction efficiency is ~ 0.08 S/m. This conductivity is consistent with that inferred from auroral observations (Saur et al., 2015). Electromagnetic induction at a single frequency provides useful constraints on the product of the conductivity and thickness of a conductor at depth but without knowing the phase lag of the induction, one cannot uniquely determine both the conductivity and the thickness of the conducting layer. However, as shown in Figure 9, if the ice thickness was 150 km and the conductivity was the same as that of the terrestrial sea water (2.75 S/m), then the ocean thickness would be ~ 4 km. If we assume the conductivity is of the order of 0.1 S/m, an ocean thicker than ~ 100 km beneath an ice shell of 150 km thickness would account for our inferred induction efficiency.

In Figure 9, color contours in the background show the phase lag of the induced field as a function of ocean conductivity and thickness. The phase lag decreases with increasing ocean conductivity and ocean thickness. For the range of ice shell thicknesses and ocean parameters that would result in a 72% induction efficiency, the corresponding phase lags are less than 20 degrees, which indicates that neglecting phase lag in our fitting of the induced dipole is a reasonable approximation.

7. Summary and Conclusions

Combining spacecraft measurements with MHD simulations, we have extracted improved estimates of Ganymede's internal field, modeling the latter as a permanent dipole moment supplemented either by an induced dipole moment or by quadrupole moments. The new approach improves the analysis of MK02 who constructed an internal field model without removing the contributions of plasma currents to the measurements. The MHD simulation results realistically

This article is protected by copyright. All rights reserved.

Author Manuscript

represent the field perturbations arising from plasma interactions. They correspond more closely to the measurements than do the sum of modeled internal fields supplemented by uniform external fields assumed in earlier work. Our approach avoids some of the problems inherent in the separation of external and internal fields when fitting data to the classical spherical harmonic expansion. For example, magnetic perturbations arising from ionospheric currents flowing below the spacecraft unavoidably combine with the magnetic signatures of truly internal current sources in the previous analysis, whereas the present approach separates the sources.

In order to extract as much information about the internal field as possible, we have added to data analyzed by MK02 the measurements made on the G8 pass, whose closest approach occurred in a region remote from those encountered on other passes and also the data from a close pass of the Juno spacecraft. The first-order internal moments derived using our new approach differ slightly from those of MK02. On the other hand, the newly fitted dipole moments are quite consistent with each other for the different model combinations. The dipole coefficients have equatorial surface strengths between 720 nT and 727 nT, slightly larger than that found by MK02 (719 nT), and nearly the same dipole tilt (~ 176°) relative to the spin axis, rotated from the Jupiter-facing meridian by slightly smaller angles (11° and 15°) towards the trailing hemisphere.

The *rms* errors of fits to a fixed dipole moment plus an induced dipole or a fixed dipole plus quadrupole differ little and do not provide a basis for selecting between the two ways of representing the internal magnetic properties of Ganymede. Indeed, it is probable that both quadrupole moments and induced moments contribute to the measured signal, and thus our estimate of the efficiency of induction could be either an underestimate or an overestimate. We cannot assert that we have established the true level of induction efficiency, nor do we believe that there is any way of doing so on the basis of data available at this time. However, the evidence that induction superimposed on a steady internal dipole field can provide a good fit to the data seems to us to suggest that it contributes the dominant signal because it would be quite fortuitous for the symmetries imposed by induction to correspond so closely to the symmetries arising from internal moments and for a single parameter to achieve nearly the same quality of model fit as a five-parameter model. The remarks that follow assume that our analysis has provided an estimate of induction efficiency that is reasonably close to realistic.

The induction efficiency remains close to 70% whether we fit three passes (MagModel1) or five passes (MagModel3). This is to be expected because Ganymede was near the magnetic equator (see Figure 2b), a node of the driving field, on both of the passes added in MagModel3 (G8 and Juno G34). The 72% efficiency that we deduce is smaller than the 84% obtained by MK02. A decreased induction efficiency can be interpreted in several ways. Possibly the conducting layer is more deeply buried than previously suggested (~ 150 km) or possibly the conductance is smaller than previously suggested or possibly some combination of these two changes is called for. In light of the recent Juno microwave measurements of the ice shell thickness (Brown et al., 2023), our results support the suggestion that the electrical conductivity of the ocean is smaller than previously proposed.

The magnetic field measurements at Ganymede were acquired on a small number of flybys, which provided limited latitude and longitude coverage of the moon's near environment. Figure

This article is protected by copyright. All rights reserved.

Author Manuscript

2a shows that no data were acquired close to Ganymede in one latitude/longitude quadrant, i.e., the leading/southern hemisphere. A magnetic anomaly localized in this region would have been "invisible". Even if the external plasma currents were fully characterized, the sparsity of data would remain a source of uncertainty. A complete determination of Ganymede's internal field requires more magnetic field measurements from future missions designed to obtain the data necessary to distinguish between permanent internal quadrupole moments and an induced dipole moment and to cover the unexplored regions, especially the southern high-latitude region. Ideally one would hope to constrain both the thickness and the conductivity of the conducting layer. As suggested by Khurana et al. (2002) for the case of Europa, measurements of magnetic induction at multiple frequencies would reveal much about the magnetic properties of Ganymede. Fortunately, the Juice spacecraft, now en route to Jupiter, will make long-term, continuous magnetic field observations at Ganymede and the Europa Clipper will also provide data from some close passes. Analysis of signals with global coverage at multiple frequencies, including the low frequency signal arising from the moon's orbital eccentricity and local time asymmetries of the Jovian magnetosphere, will undoubtedly distinguish between the models that we consider here and greatly reduce remaining uncertainties. It seems likely that even after new data become available, self-consistent global simulations of Ganymede's magnetosphere will continue to play a key role in interpreting existing observations and fully characterizing the magnetic properties of Ganymede.

Acknowledgements

We are most grateful to John E. P. Connerney for his helpful suggestions for improvement of earlier versions of this paper. Hao Cao's wise queries greatly helped us improve our analysis. We would also like to thank the two reviewers for their constructive and thoughtful comments, which have helped improve the paper. XJ acknowledges support by NASA through Early Career Fellow Startup Grant #80NSSC20K1286 and JUICE/PEP contract #183512 with JHU/APL.

Data Availability

The Galileo and Juno magnetic field data used in this work are publicly available at the PPI node of the Planetary Data System through Kivelson et al. (2024) and Connerney (2024). Data files containing the MHD-modeled magnetic fields used in this work are available in Jia (2024).

This article is protected by copyright. All rights reserved.

Author Manuscript

Author Manuscript

References

Acuna, M. H., Connerney, J. E. P., Wasilewski, P., Lin, R. P., Mitchell, D., Anderson, K. A. et al. (2001), Magnetic field of Mars: Summary of results from the aerobraking and mapping orbits, *J. Geophys. Res*. 106, 23,403-23,417.

Allegrini, F., Bagenal, F., Ebert, R. W., Louarn, P., McComas, D. J., Szalay, J. R., et al. (2022). Plasma observations during the 7 June 2021 Ganymede flyby from the Jovian Auroral Distributions Experiment (JADE) on Juno. Geophysical Research Letters, 49, e2022GL098682. https://doi.org/10.1029/2022GL098682.

Brown, S., Zhang, Z., Bolton, S., Bonnefoy, L. E., Ermakov, A., Feng, J., et al. (2023). Microwave observations of Ganymede's sub-surface Ice: I. Ice temperature and structure. *Journal of Geophysical Research: Planets*, 128, e2022JE007609. https://doi.org/10.1029/2022JE007609.

Chapman, S. and Bartels, J. (1940), *Geomagnetism*, Clarendon Press, Oxford, London.

Christensen, U. R. (2015), Iron snow dynamo models for Ganymede, *Icarus*, 247, 248 – 259.

Connerney, J. (2017). Juno MAG calibrated data j v1.0, JNO-j-3-FGM-CAL-v1.0. *NASA Planetary Data System*. https://doi.org/10.17189/1519711.

Connerney, J. E. P., Benn, M., Bjarno, J. B., Denver, T., Espley, J., Jorgensen, J. L., et al. (2017). The Juno magnetic field investigation. *Space Science Reviews*, 213(1–4), 39–138. https://doi.org/10.1007/s11214-017-0334-z.

Connerney, J.E.P., Timmins, S., Herceg, M., & Joergensen, J. L., (2020). A Jovian magnetodisc model for the Juno era. *Journal of Geophysical Research: Space Physics*, 125, https://doi:10.1029/2020JA028138.

Connerney, J. E. P., Timmins S., Oliversen R. J., et al. (2022). A new model of Jupiter's magnetic field at the completion of Juno's prime mission. *J Geophys Res, Planets,* 127(2):e07055. https://doi.org/10.1029/2021JE007055.

Connerney, J. E. P. (2024), Juno MAG CALIBRATED DATA J V1.0, JNO-J-3-FGM-CAL-V1.0, NASA Planetary Data System. https://doi.org/10.17189/1519711.

Duling, S., Saur, J., Clark, G., Allegrini, F., Greathouse, T., Gladstone, R., et al. (2022). Ganymede MHD model: Magnetospheric context for Juno's PJ34 flyby. *Geophysical Research Letters*, 49(24), e2022GL101688. https://doi.org/10.1029/2022GL101688.

Fatemi, S., A. R. Poppe, K. K. Khurana, M. Holmstr.m, and G. T. Delory (2016), On the formation of Ganymede's surface brightness asymmetries: Kinetic simulations of Ganymede's magnetosphere, *Geophys. Res. Lett*., 43, doi:10.1002/2016GL068363.

This article is protected by copyright. All rights reserved.

Gurnett, D. A., Kurth, W. S., Roux, A., Bolton, S. J., and Kennel, C. F. (1996), Evidence for a magnetosphere at Ganymede from plasma wave observations by the Galileo spacecraft, *Nature*, 384, 535-537.

Hansen, C. J., Bolton, S., Sulaiman, A. H., Duling, S., Bagenal, F., Brennan, M., et al. (2022). Juno's close encounter with Ganymede - An overview. *Geophys. Res. Lett.*, 49, e2022GL099285. https://doi.org/10.1029/2022GL099285.

Jia, X., Walker, R. J., Kivelson, M. G., Khurana, K. K., and Linker, J. A. (2008), Three dimensional MHD simulations of Ganymede's magnetosphere, *J. Geophys. Res.*, Vol. 113, doi:10.1029/2007JA012748.

Jia, X., Walker, R. J., Kivelson, M. G., Khurana, K. K., & Linker, J. A. (2009). Properties of Ganymede's magnetosphere inferred from improved three-dimensional MHD simulations. *J. Geophys. Res.*, 114(A9). doi:10.1029/2009JA014375.

Jia, X., Kivelson, M. G., Khurana, K. K. and Walker, R. J. (2010a), Magnetic fields of the satellites of Jupiter and Saturn, *Space Sci. Rev*., doi:10.1007/s11214-009-9507-8.

Jia, X., Walker, R. J., Kivelson, M. G., Khurana, K. K., & Linker, J. A. (2010b). Dynamics of Ganymede's magnetopause: Intermittent reconnection under steady external conditions. *J. Geophys. Res.*, 115(A12). doi:10.1029/2010JA015771.

Jia, X., & Kivelson, M. G. (2021). The magnetosphere of Ganymede. in *Space Physics and Aeronomy Collection Volume 2: Magnetospheres in the Solar System, Geophysical Monograph 259*, First Edition (edt. R. Maggiolo, N. André, H. Hasegawa, and D. T. Welling), Wiley, doi: 10.1002/9781119507512.

Jia, X. (2024), Data for "Improved Models of Ganymede's Permanent and Induced Magnetic Fields based on Galileo and Juno Data" by Jia et al. (2024) [Data set], *University of Michigan - Deep Blue Data*, https://doi.org/10.7302/rm5c-tm17.

Khurana, K. K., Kivelson, M. G., Stevenson, D. J. et al. (1998). Induced magnetic fields as evidence for subsurface oceans in Europa and Callisto. *Nature*, 395, 749

Khurana, K. K., Kivelson, M. G., and C. T. Russell (2002), Searching for liquid water in Europa by using surface observatories, *Astrobiology*, 2(1), 93-103, doi: 10.1089/ 153110702753621376.

Khurana, K. K., X. Jia, M.G. Kivelson, F. Nimmo, G. Schubert and C.T. Russell (2011), Evidence of a global magma ocean in Io's interior, *Science*, 332, 1186, doi: 10.1126/Science. 1201415.

Kivelson, M. G., Khurana, K. K., Means, J. D. et al. (1992), The Galileo magnetic field investigation. *Space Sci. Rev*., 60, 357–383. https://doi.org/10.1007/BF00216862.

Kivelson, M. G., Khurana, K. K., Russell, C. T., Walker, R. J., Warnecke, J., Coroniti, F. V., Polanskey, C. Southwood, D. J. and Schubert, G. (1996), Discovery of Ganymede's magnetic field by the Galileo spacecraft, *Nature*, 384, 537 - 541.

This article is protected by copyright. All rights reserved.

Author Manuscript

Kivelson, M. G., Khurana, K., Coroniti, F., Joy, S., Russell, C., Walker, R., et al. (1997). The magnetic field and magnetosphere of Ganymede. *Geophys. Res. Lett.*, 24(17), 2155–2158. https://doi.org/10.1029/97gl02201.

Kivelson, M. G., Khurana, K. K. and Volwerk, M. (2002), The permanent and inductive magnetic moments of Ganymede, *Icarus*, 157, 507-522.

Kivelson, M. G., Khurana, K. K., Russell, C. T., Walker, R. J., Joy, S. P., and Mafi, J. N. (2024). Galileo Orbiter at Jupiter Magnetometer High Resolution Calibrated Bundle, *NASA Planetary Data System*. https://doi.org/10.17189/1gfw-1y75.

Korth, H., Anderson, B. J., Acuña, M. H., Slavin, J. A., Tsyganenko, N. A. Solomon, S. C. and McNutt R. L. (2004), Determination of the properties of Mercury's magnetic field by the MESSENGER mission, *Planet. Space Sci*., 52, 733-746, doi:10.1016/j.pss.2003.12.008.

Langel, R. A. (1987), The main field, in *Geomagnetism*, Vol. 1, edited by J. A. Jacobs, pp. 249 - 512, Academic Press, London.

Neubauer, F. M. (1978), Possible strengths of dynamo magnetic fields of the Galilean satellites and of Titan. *Geophys. Res. Lett*., 5, 905 - 908. doi:10.1029/GL005i011p00905.

Olsen, N., Glassmeier, K.-H. and Jia, X. (2010), Separation of the magnetic field into external and internal parts, *Space Sci. Rev*., Vol. 152, issue 1, doi:10.1007/s11214-009-9563-0.

C. Paty, R. Winglee (2006), The role of ion cyclotron motion at Ganymede: magnetic morphology and magnetospheric dynamics. *Geophys. Res. Lett*. 33, L10106. doi:10.1029/2005GL025273.

Phillips, J. L. and Russell, C. T. (1987), Upper limit on the intrinsic magnetic field of Venus, *J. Geophys. Res.*, 92, 2253-2263.

Plattner, A. M., et al. (2023), On Ganymede's Magnetic Quadrupolar Strength, *Planet. Sci. J*., 4, 134, doi:10.3847/PSJ/acde7f.

Romanelli, N., DiBraccio, G. A., Modolo, R., Connerney, J. E. P., Ebert, R. W., Martos, Y. M., et al. (2022). Juno magnetometer observations at Ganymede: Comparisons with a global hybrid simulation and indications of magnetopause reconnection. *Geophysical Research Letters*, 49(23), e2022GL099545. https://doi.org/10.1029/2022GL099545.

Russell, C. T., Coleman, P. J., Jr., and Schubert, G. (1974), Lunar magnetic field: Permanent and induced dipole moments, *Science, 186*, 825-6. doi: 10.1126/science.186.4166.82

Russell, C.T. (1980), Planetary magnetism, *Reviews of Geophysics*, v. 18, p. 77–106.

Saur, J., et al. (2015), The search for a subsurface ocean in Ganymede with Hubble Space Telescope observations of its auroral ovals, *J. Geophys. Res. Space Physics*, 120, doi:10.1002/2014JA020778.

This article is protected by copyright. All rights reserved.

Author Manuscript

Schubert, G., Spohn, T. and Reynolds, R. T. (1986), Thermal histories, compositions and internal structures of the moons of the solar system, in *Satellites*, edited by J. A. Burns and M. S. Matthews, pp. 224-292, University of Arizona Press, Tucson.

Schubert, G., Zhang, K., Kivelson, M. G., and Anderson, J. D. (1996), The magnetic field and internal structure of Ganymede, *Nature*, 384, 544 -545.

Seufert, M., J. Saur, and F. M. Neubauer (2011), Multi-frequency electromagnetic sounding of the Galilean moons, *Icarus*, Volume 214, Issue 2, Pages 477-494.

Stahl, A., Addison, P., Simon, S., & Liuzzo, L. (2023). A model of Ganymede's magnetic and plasma environment during the Juno PJ34 flyby. *Journal of Geophysical Research: Space Physics*, 128, e2023JA032113. https://doi.org/10.1029/2023JA032113.

Weber, T., Moore, K., Connerney, J., Espley, J., DiBraccio, G., and Romanelli, N. (2022). Updated spherical harmonic magnetic field moments of Ganymede from the Juno flyby. *Geophys. Res. Letts.*, 49, e2022GL098633. https://doi.org/10.1029/2022GL098633

Wei, H. Y., Russell, C. T., Dougherty, M. K., Neubauer, F. M. and Ma, Y. J. (2010), Upper limits on Titan's magnetic moment and implications for its interior, *J. Geophys. Res.*, 115, E10007, doi:10.1029/2009JE003538.

Toth, G., Jia, X., Markidis, S., Peng, I. B.,Chen, Y. Daldorff, L. K. S., et al., (2016), Extended magnetohydrodynamics with embedded particle-in-cell simulation of Ganymede's magnetosphere, *J. Geophys. Res.*, doi:10.1002/2015JA021997.

Zhou, H., G. Toth, Jia, X., Chen, Y. & Markidis, S. (2019), Embedded kinetic simulation of Ganymede's magnetosphere: Improvements and inferences, *J. Geophys. Res.*, doi:10.1029/2019JA026643.

Zhou, H., G. Toth, X. Jia, and Y. Chen (2020), Reconnection-driven dynamics at Ganymede's upstream magnetosphere: 3D global Hall MHD and MHD-EPIC simulations, *Journal of Geophysical Research – Space Physics*, doi:10.1029/2020JA028162.

Zimmer, C., Khurana, K. K. and Kivelson, M. G. (2000), Subsurface oceans on Europa and Callisto: Constraints from Galileo magnetometer observations, *Icarus*, $147(2),329-347$, doi:10.1006/ icar.2000.6456.

This article is protected by copyright. All rights reserved.

Author Manuscript

Tables

Table 1. Time within 2 R_G of Ganymede's center of mass on spacecraft passes by Galileo and Juno, the range of *B* (maximum minus minimum value) encountered, altitude of closest approach, and SIII (west) longitude of Ganymede at the time of encounter

	G1	G2	G7	G8	G28	G29	Juno G34
Time (min) within 2R_G	22	19	0	12	12	6	7
Range of *B*(nT)	359	1060	-	75	290	55	205
Closest approach altitude (km)	835	261	-	1603	809	2338	355
SIII (west) longitude or synodic phase (°)	175	158	20	287	352	220	302

This article is protected by copyright. All rights reserved.

Table 2. Internal field parameters from different models and from MK02

	Model	Dipole coefficients				Ind [a]	Quadrupole coefficients					*rms* error [nT]						
		g_1^0	g_1^1	h_1^1	M [b]		g_2^0	g_2^1	g_2^2	h_2^1	h_2^2	G1	G2	G8	G28	Juno G34	**Total *rms* [c]**	**Total weighted *rms* [d]**
Dipole + Induction	**MK02** (G1, G2, G28)	-716.8	49.3	22.2	718.8	0.84						9.8	7.5		15.6		**11.5**	**13.2**
	MagModel1 (G1, G2, G28)	-722.6	43.6	7.5	724.0	0.72 ±0.03						11.7	12.0		10.2		**11.4**	**10.8**
	MagModel3 (G1, G2, G8, G28, Juno G34)	-718.6	46.3	12.2	720.2	0.71 ±0.03						11.5	13.7	10.8	10.5	9.1	**11.4**	**10.7**
Dipole + Quadrupole	**MK02** (G1, G2, G28)	-711.0	46.8	22.3	712.9		0.9	27	-0.4	1.8	-11	11.9	15.6		13.2		**13.5**	**12.6**
	MagModel2 (G1, G2, G28)	-732.6	36.6	2.0	733.5		19.7	11.9	-22.5	28.4	-14.2	7.7	20.1		7.3		**12.9**	**8.5**
	MagModel4 (G1, G2, G8, G28, Juno G34)	-725.6	35.7	6.9	726.5		3.8	31.9	-9.8	13.5	-5.4	10.3	17.8	10.7	8.4	8.3	**11.8**	**10.1**

[a.] "Ind" denotes the induction efficiency.

[b.] Dipole moment (*M*) listed here gives the equatorial surface strength in nT.

[c.] *rms* error summed over all passes used for the fit (see equation 9).

[d.] Weighted *rms* error summed over all passes used for the fit, where weighting is inversely proportional to the maximum field strength of individual passes used for the fit (see equation 10).

[e.] Fit coefficients of MagModel1-4 correspond to the mean values of all the data points in the shaded region in Figures 5-8, respectively. The induction efficiency for MagModel1 and MagModel3 is presented with its standard deviation in the shaded region.

Author Manuscript

This article is protected by copyright. All rights reserved.

Author Manuscript

Figures and Figure Captions

Figure 1. Schematics illustrating the different sources of magnetic field at Ganymede. (a) Permanent field plus the background Jovian field; (b) Induced field plus the background Jovian field; (c) Total magnetic field including the background Jovian field, Ganymede's internal field and the magnetic field generated by plasma currents (i.e., red-yellow regions corresponding to current sheets on the upstream magnetopause and in the downsteam magnetotail) arising from the interaction between Jupiter's magnetospheric plasma and Ganymede's field. The green lines in all panels represent sampled magnetic field lines. Also shown in panels (a) and (b) are the cross-sections of Ganymede's interior consisting of an iron core, a rocky mantle and a subsurface ocean sandwiched by layers of ice.

Figure 2. (a) Plot of latitude versus longitude of the six Galileo trajectories and the Juno G34 trajectory (color-coded) in Ganymede-centered spherical coordinates. Longitude is measured from the Jupiter-facing meridian in a left-handed sense and latitude is measured from Ganymede's equator. The solid traces represent the intervals when the spacecraft was within $2R_{\mathrm{G}}$ of the center of mass of Ganymede, beyond which the internal field strength becomes less than the external field strength. (b) A schematic showing Ganymede's and Juno's locations relative to Jupiter's magnetospheric current sheet during the flybys. The G1, G2 and G29 flybys occurred well above the current sheet while the G7 and G28 flybys occurred well below the current sheet. The G8 pass and the Juno G34 pass occurred near the central current sheet.

Figure 3. Magnetic field comparisons (in GphiO coordinates) between the Galileo measurements and MHD simulations for the G2 pass. In panel (a), black solid lines are the Galileo data, green lines are the initial input in the MHD model and red traces are the simulation results. In order to account for the rapid temporal variations of Ganymede's magnetosphere resulting from reconnection on the magnetopause, simulation results shown in the comparisons are averaged over time steps that span a time interval of ~ 2 minutes after the system stabilizes. Blue dashed lines are the differences between red and green traces. They represent the perturbation fields due to the external current system identified in the MHD model. Gray shaded regions are the time intervals used by MK02 for the separation of internal-external fields. An expanded view of the components of the external fields during the marked intervals is plotted in panel (b). Figure adapted from Olsen et al. (2010).

Figure 4. Same as Figure 3 but for the G28 pass.

Figure 5. Coefficients of Ganymede's internal field modeled as a permanent dipole and an induced dipole (MagModel1). The parameters were fit to observations of the magnetic field on the G1, G2 and G28 flybys after subtraction of field perturbations arising from plasma currents. Because the G28 simulation varies as a function of run-time, we show fits that vary with simulation time step. Panels (a) to (c) show the fitted permanent dipole moments (in nT) in terms of g10, g11 and h11

This article is protected by copyright. All rights reserved.

defined in the text and panel (d) shows the induction efficiency. In these panels, blue dashed lines mark the values reported by MK02. Panel (e) shows the *rms* errors of the fit for the G1 (black), G2 (magenta) and G28 (green) flybys. The total *rms* errors (in nT) are shown for both the new fit (red) and the model of MK02 (blue). The grey shaded region marks the interval during which the fitted parameters appear to converge to asymptotic values.

Figure 6. Same as Figure 5 but for an internal field model of a dipole plus a quadrupole.

Figure 7. Same format as Figure 5 but based on data from the G1, G2, G8, G28 and Juno G34 passes. Model results of MagModel3 are represented by black asterisks. Results of MagModel1 and MK02 are shown as red dots and blue dashed lines, respectively.

Figure 8. Fits from MagModel4 based on data from the G1, G2, G8, G28 and Juno G34 passes. Model results are represented by black asterisks. Results of MagModel2 and MK02 are shown as red dots and blue dashed lines, respectively.

Figure 9. The ocean thickness (in km) as a function of the ocean conductivity (in S/m) that produce an induced field of normalized amplitude A= 0.72 at the synodic period of Ganymede (10.5 hours). The colored curves correspond to different ice shell thicknesses (or burial depths of the ocean), *d,* ranging from d = 25 km (leftmost curve) to d = 250 km (rightmost curve) at 25 km increments. The magenta curve highlights the case for an ice shell thickness of 150 km. The color contours in the background indicate the phase lag (in degrees) of the induced field as a function of ocean conductivity and thickness.

Author Manuscript

This article is protected by copyright. All rights reserved.

Author Manuscript

Appendix

The presently available data for Ganymede's magnetic field limits our ability to uniquely retrieve internal field parameters. We can gain insight into the non-uniqueness of the solution from our inversion by examining the correlation coefficients between different model parameters. Figure A1 maps the correlation coefficients for the two classes of models used in our analysis: (Left) permanent dipole plus induced dipole and (Right) permanent dipole plus quadrupole.

The off-diagonal correlation coefficients for the permanent plus induced dipole model do not exceed 0.28 (Figure A1-left). Fits distinguish the two sources clearly, undoubtedly because of the time-dependent nature of the induced dipole moment. In contrast, significant correlations are present between pairs of multipole moments (Figure A1-Right), indicating that the fits using multipoles (through order 2) are poorly constrained by the data.

We do not provide a fit using a permanent dipole and both quadrupolar terms and induction, but we show in Figure A2 the correlation coefficients for such a model. The strong correlation between g_2^1 and induction (0.63) makes clear that such a fit is too poorly constrained to be meaningful.

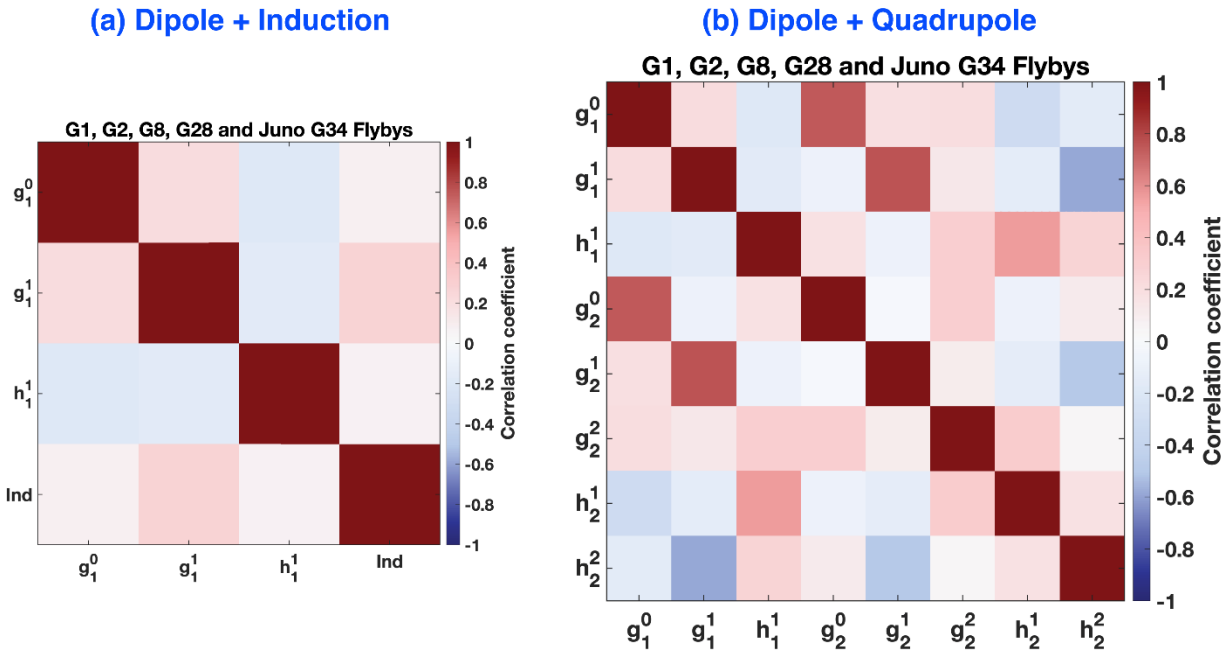


Figure A1. Maps the correlation coefficients among the various internal field model parameters used to represent Ganymede's internal field. (Left) Permanent and induced dipole terms. (Right) Permanent dipole and quadrupole terms. The correlation coefficients are calculated using the data from the Galileo G1, G2, G8, G28 flybys and the Juno G34 flyby.

This article is protected by copyright. All rights reserved.

Author Manuscript

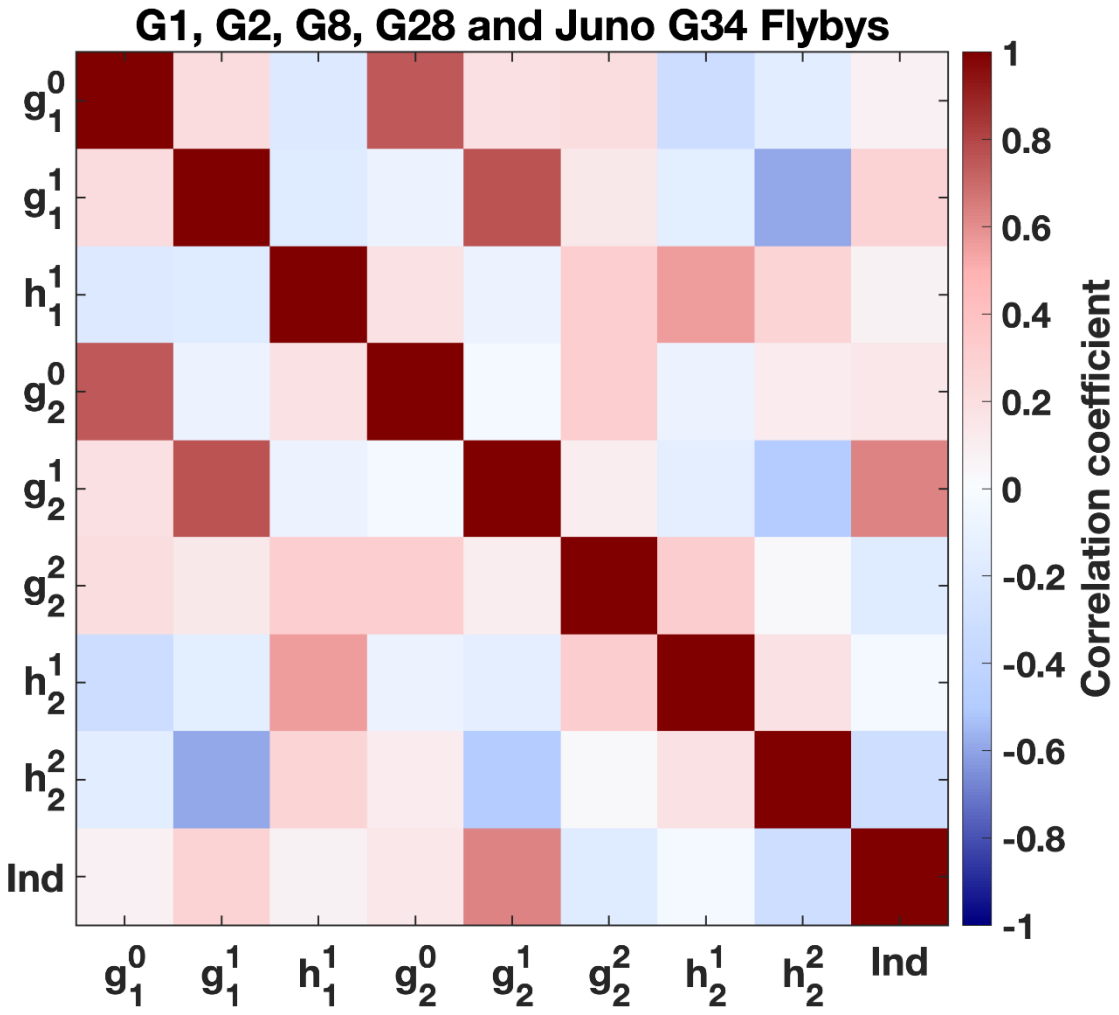
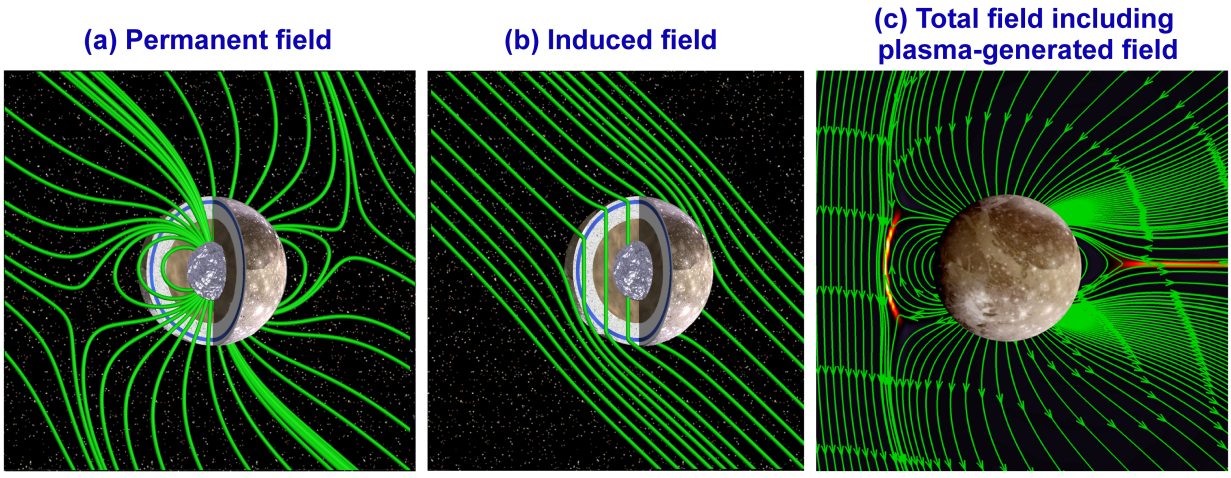


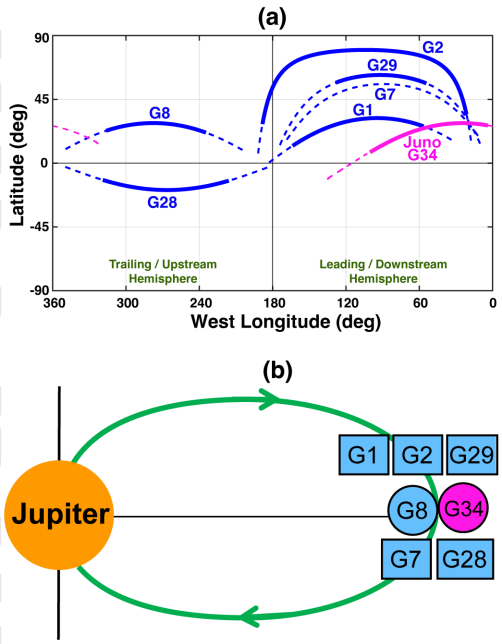
Figure A2. Same as Figure A1 but for an internal field model that includes a permanent dipole, a quadrupole and an induced dipole.

This article is protected by copyright. All rights reserved.

Author Manuscript

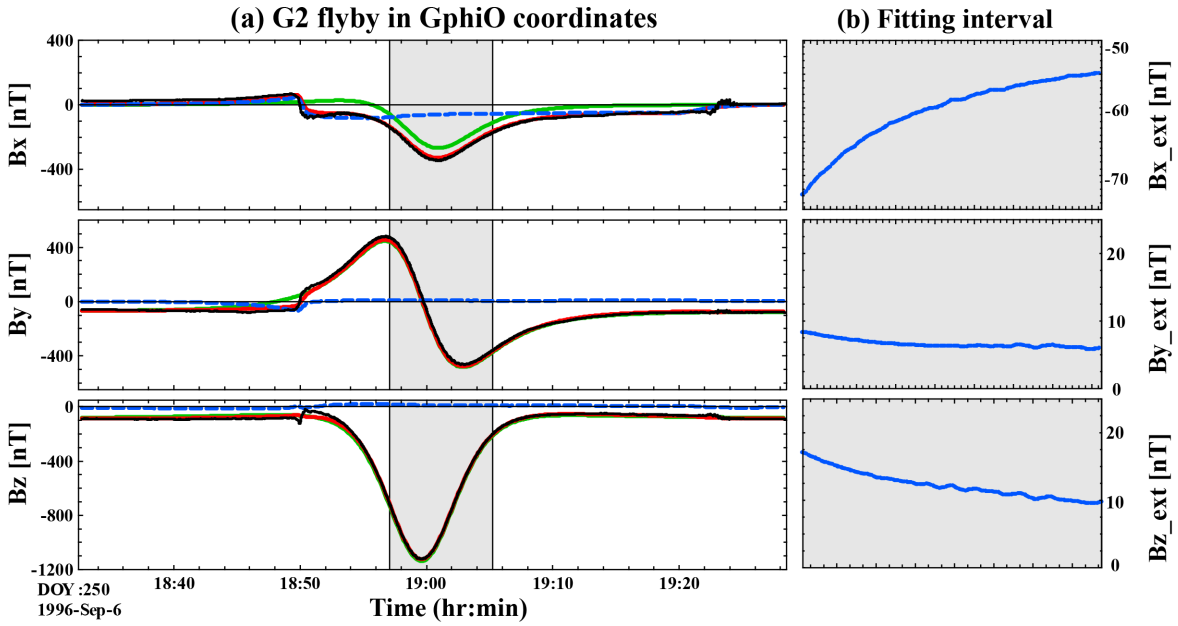


This article is protected by copyright. All rights reserved.



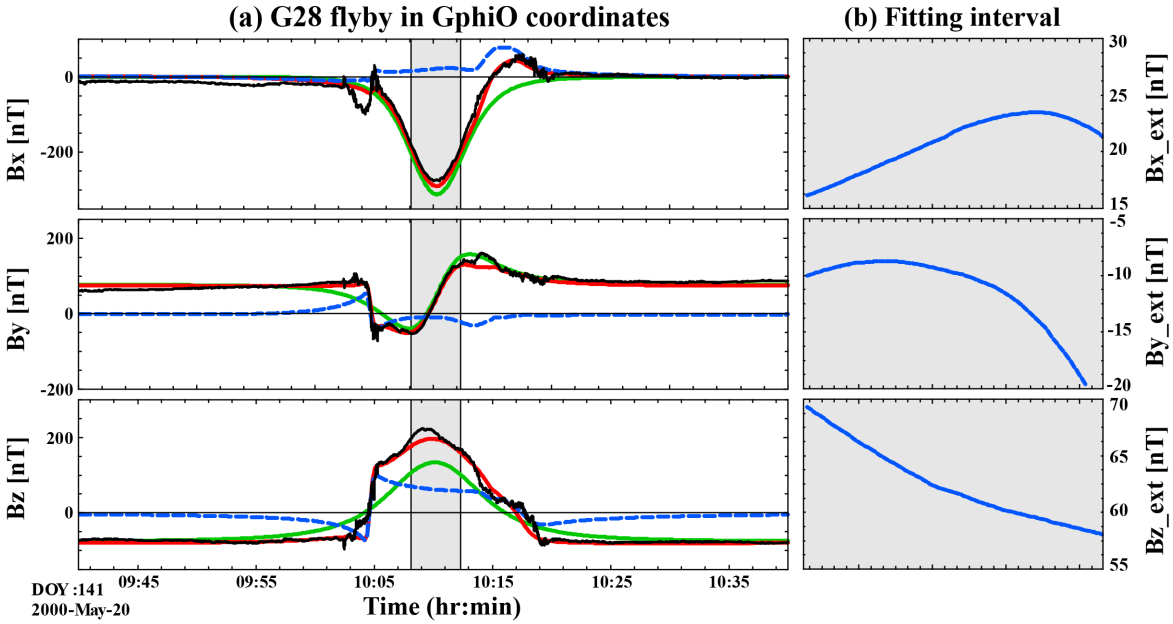
Author Manuscript

This article is protected by copyright. All rights reserved.



Author Manuscript

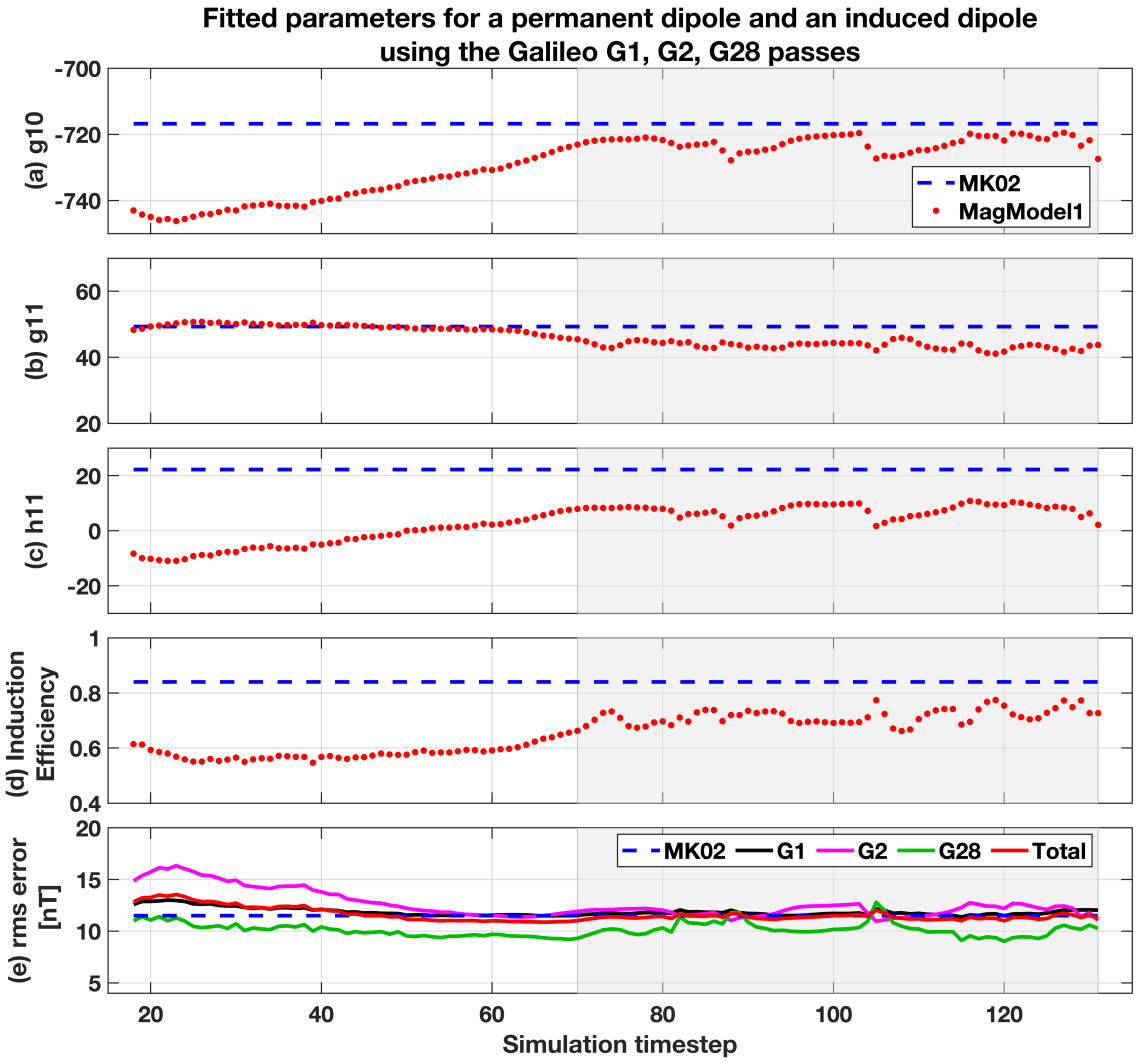
This article is protected by copyright. All rights reserved.



Author Manuscript

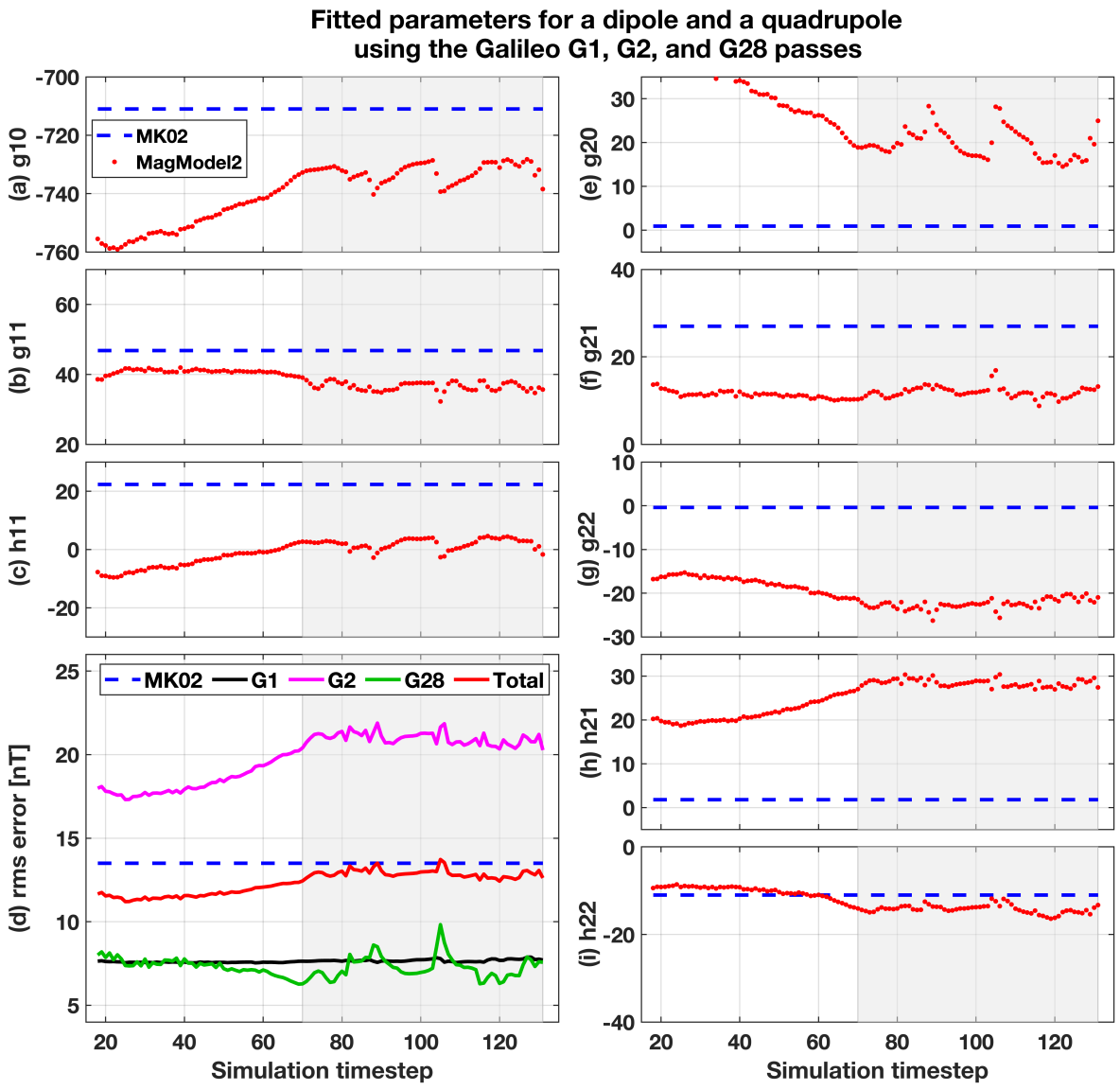
This article is protected by copyright. All rights reserved.

Author Manuscript



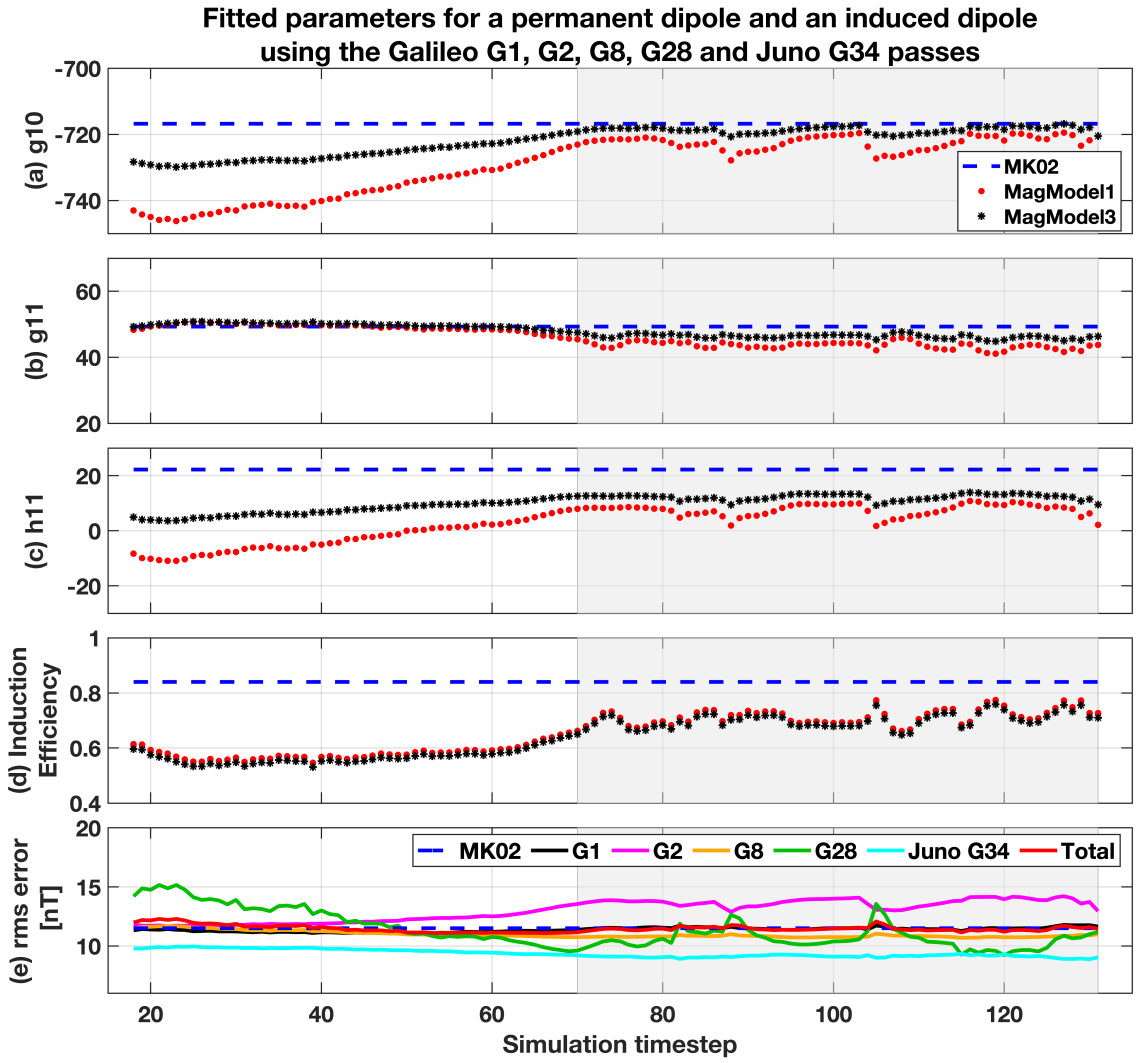
This article is protected by copyright. All rights reserved.

Author Manuscript



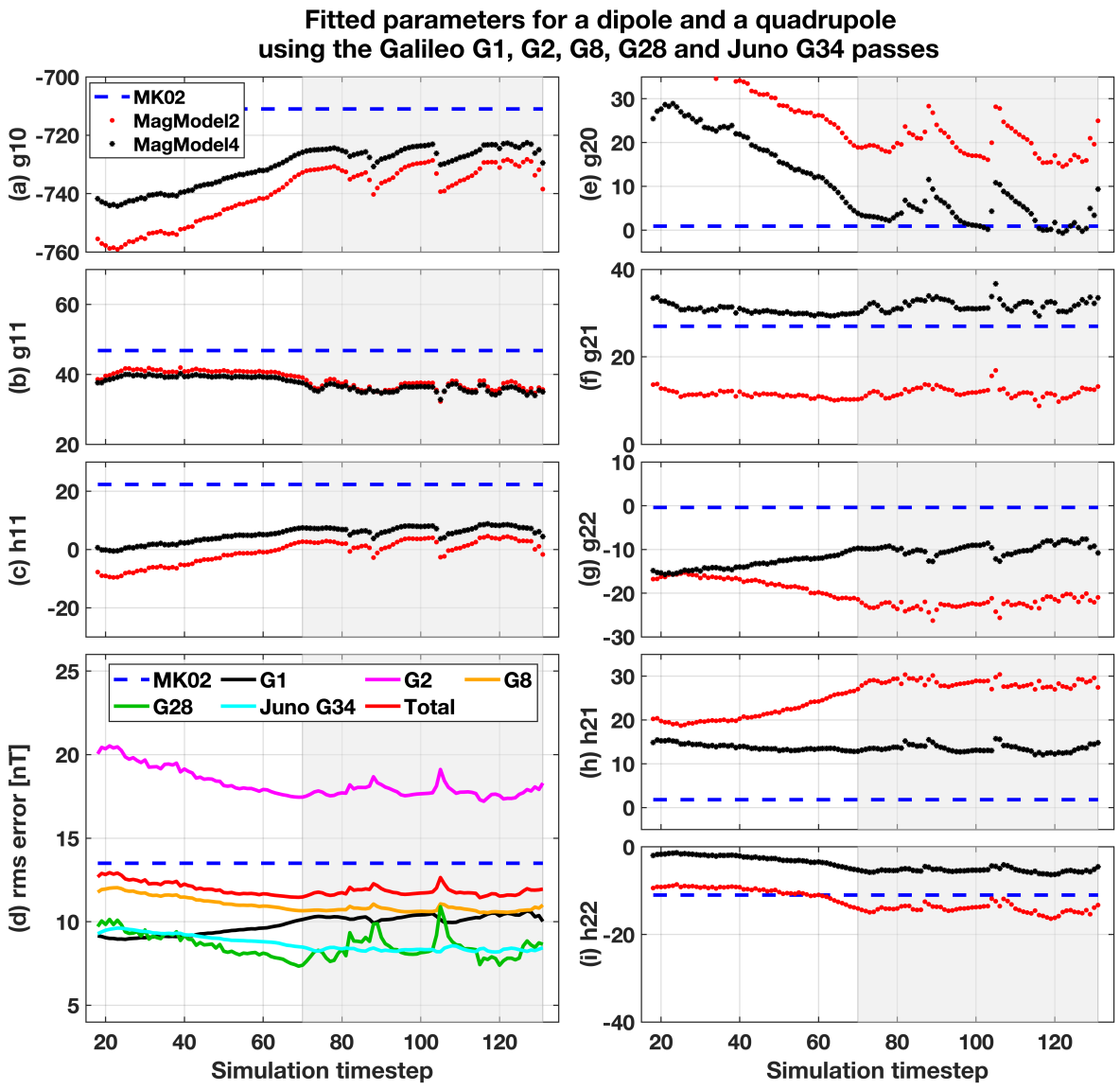
This article is protected by copyright. All rights reserved.

Author Manuscript



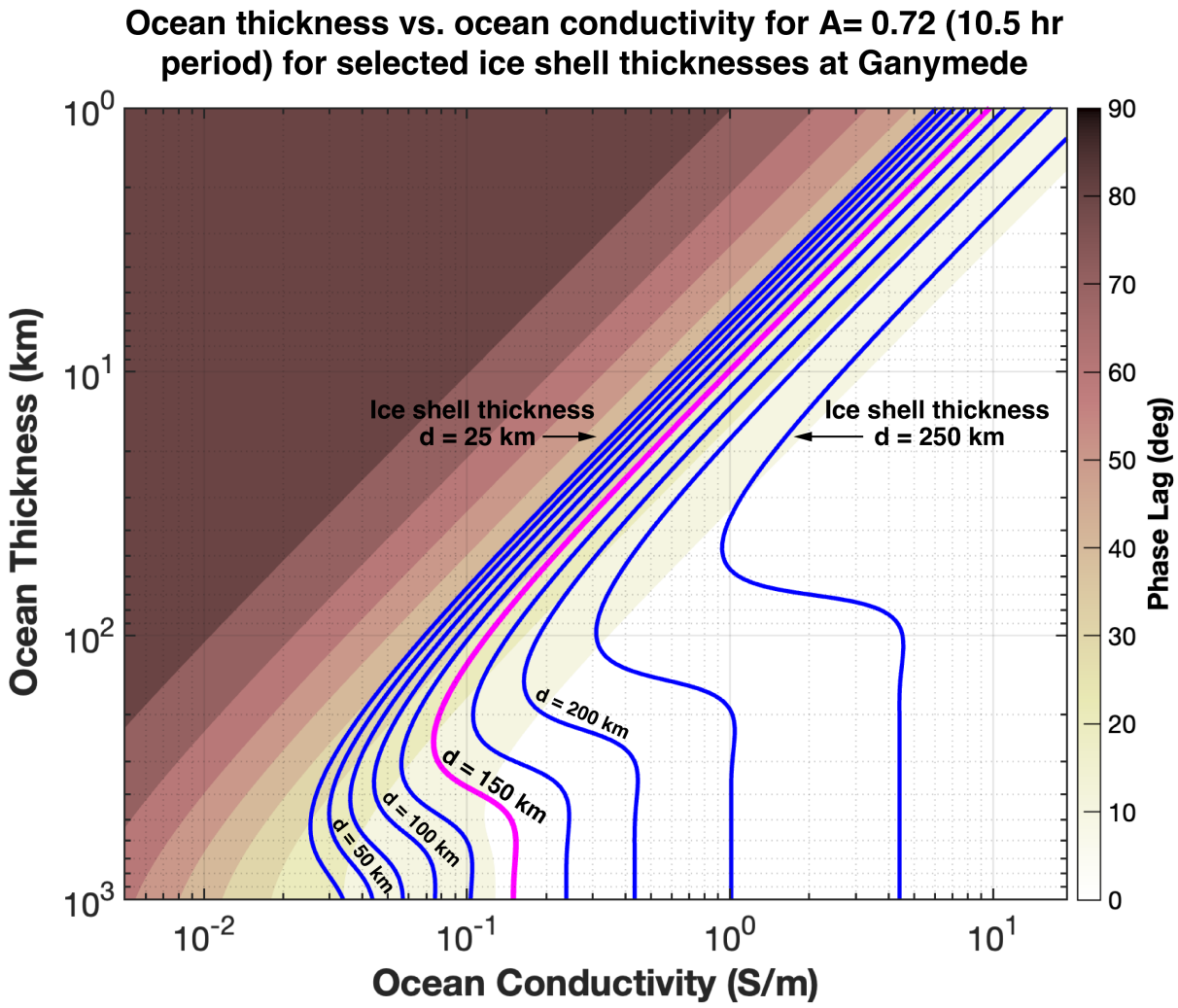
This article is protected by copyright. All rights reserved.

Author Manuscript



This article is protected by copyright. All rights reserved.

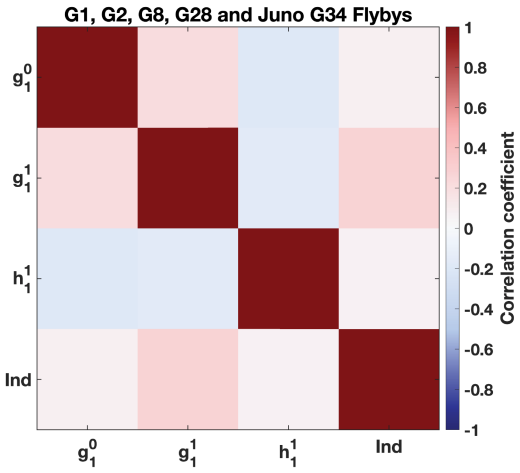
Author Manuscript



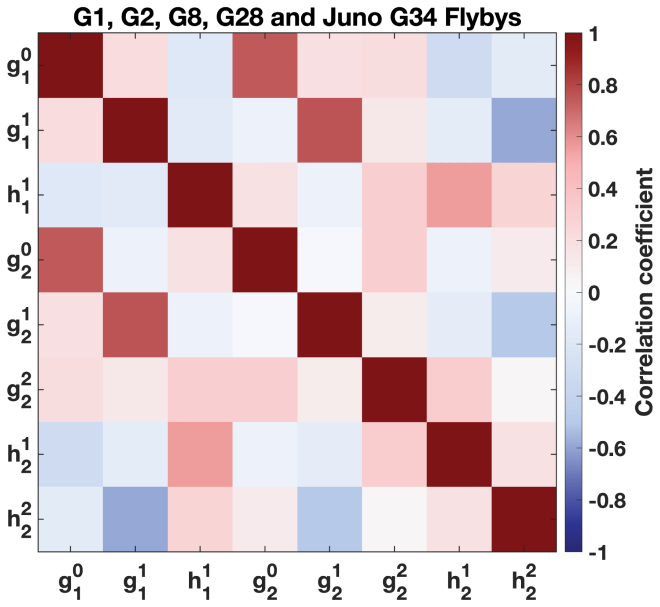
This article is protected by copyright. All rights reserved.

Author Manuscript

(a) Dipole + Induction

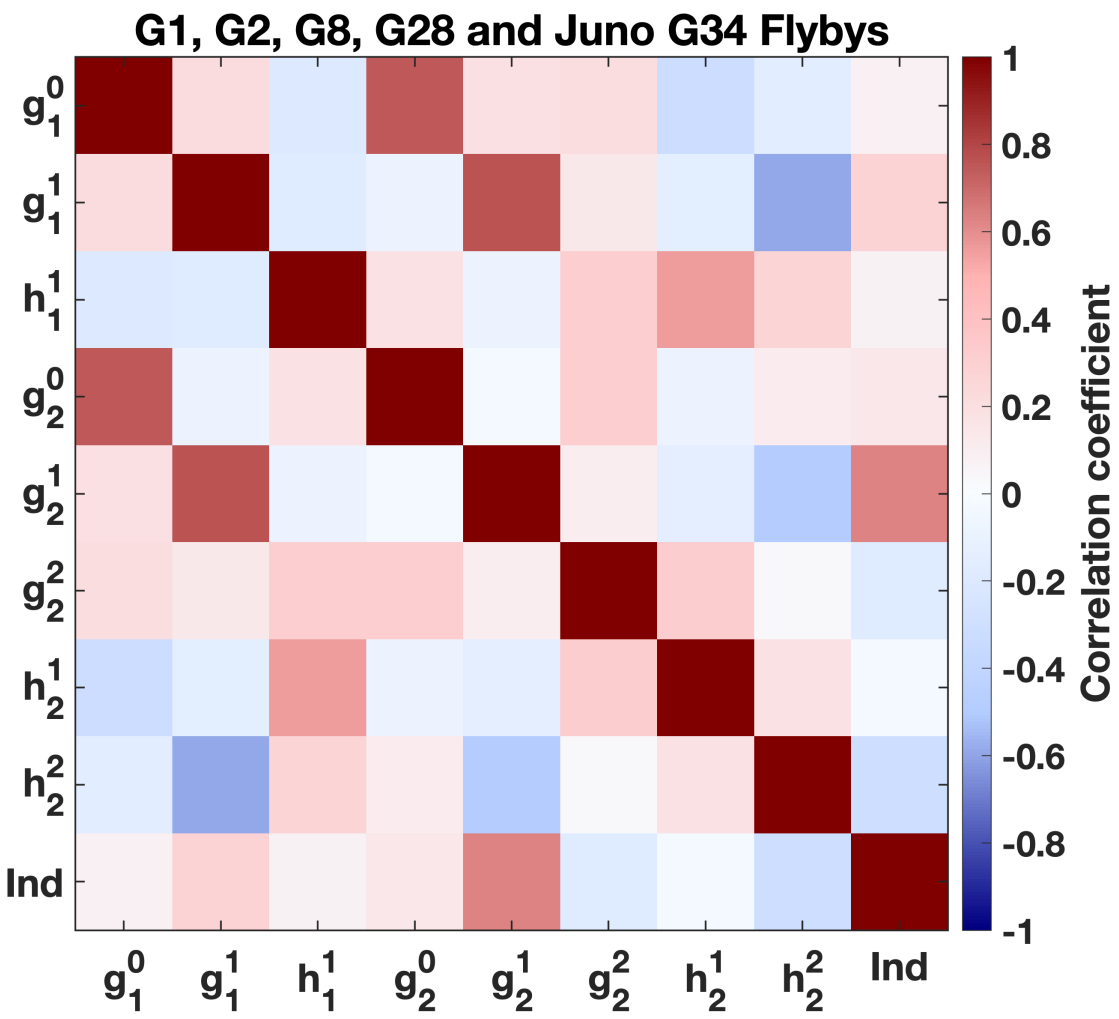


(b) Dipole + Quadrupole



This article is protected by copyright. All rights reserved.

Author Manuscript



This article is protected by copyright. All rights reserved.